NUMERICAL INVESTIGATION OF THE IMPACT OF WASHCOAT DISTRIBUTION ON THE FILTRATION PERFORMANCE OF GASOLINE PARTICULATE FILTERS

Igor Belot[1], David Vidal[1], Martin Votsmeier[2], Robert E. Hayes[3] and François Bertrand[1*]

[1]Research Unit for Industrial Flow Processes (URPEI), Department of Chemical Engineering, Polytechnique Montréal, Montreal, QC, Canada H3C 3A7

[2]UMICORE – Research and Development, Hanau, Germany

[3]Department of Mechanical Engineering, University of Alberta, Edmonton, AB, Canada T6G 2G6

[*] Corresponding author: francois.bertrand@polymtl.ca

Abstract: A three-step numerical model sheds light on the impact of three-way catalyst (TWC) washcoat distribution within the cordierite porous wall of a clean gasoline particulate filter (GPF) on its filtration performance. The model relies on (1) the numerical reconstruction of porous wall sections with various washcoat distributions and coating amounts, generated using a novel set of erosion/dilation-based procedures applied on segmented X-ray computed tomography data, (2) the computation of the flow field using the lattice Boltzmann method, and (3) the prediction of soot capture efficiency by solving the Langevin equation. The impact of washcoat distribution and amount on the pressure drop, permeability, filtration efficiency, and filter quality factor is systematically investigated. For a non-uniform washcoat distribution, an unexpected decrease in filtration efficiency with an increase in washcoat amount is explained and this highlights the complexity of the effects generated by the deposition of washcoat within the porous wall of the filter.

Keywords: Gasoline particulate filter, three-way catalyst uniformity, soot filtration, structure reconstruction, porous media, lattice Boltzmann method.

1. INTRODUCTION

With up to 25% improved fuel efficiency and performance as well as reduced greenhouse gas emissions compared to traditional gasoline port fuel injection engines (Zhao, Lai, and Harrington 1999), gasoline direct injection (GDI) engines have been rapidly adopted by automotive manufacturers and consumers. This technology has captured over 50% and 43% of the gasoline passenger car market share as of 2016 in the USA and EU, respectively, only nine years after its worldwide introduction (Joshi and Johnson 2018; Davis et al. 2016; "European Vehicle Market Statistics" 2017). Although GDI engine particulate emissions account for only about 1% of the total particle number emitted by diesel engines, they are not as benign as they seem since they often peak at diameters around 30 nm (Braisher, Stone, and Price 2010; Platt et al. 2017; Zinola et al. 2013). At these particle sizes, soots are much more difficult to remove from exhaust gases and can penetrate much more deeply into the lungs (Lewtas 2007). In addition to soot particles, nitrogen oxide (NO_X), hydrocarbon (HC), and carbon monoxide (CO) emissions are also of particular concern to OEMs (Zhao, Lai, and Harrington 1999). To comply with increasingly stringent pollutant emission regulations such as Euro 6 (Richter et al. 2012; Inoda et al. 2017), automotive OEMs must develop improved exhaust gas aftertreatment devices.

Particulate filters (PF) were originally introduced to reduce diesel engine particulate matter (PM) emissions. PFs consist of a honeycomb structure of parallel channels alternately closed at the inlet and outlet. Their walls are made of a porous material such as cordierite or silicon carbide (SiC) (Guan et al. 2015), as shown in Figure 1. In parallel, catalytic converters have been developed to reduce NO_X, CO, and HC gas emissions (Wang et al. 2014). They consist of a monolith containing open channels covered with a catalytic washcoat.

In recent years, researchers have become increasingly interested in combining the two units into a catalyst-coated PF (CPF), which consists of depositing a catalytic washcoat directly on or within the porous wall of the filter. Many techniques have been reported in the literature to achieve this result. The most common method involves injecting a dispersion coating into the PF and then drying the catalyst carrier afterwards (Shimrock, Taylor, and John M. Collins 1985; Aderhold et al. 1999; Foerster et al. 2000). CPFs have the advantage of removing soot particles at the same time as CO, HC, and NO_X gases, while gaining space, improving effectiveness, and reducing costs and

overall pressure drop. In the case of a diesel particulate filter (DPF), a selective catalytic reduction (SCR) coating (Thomas et al. 2019), is usually applied to the filter wall.

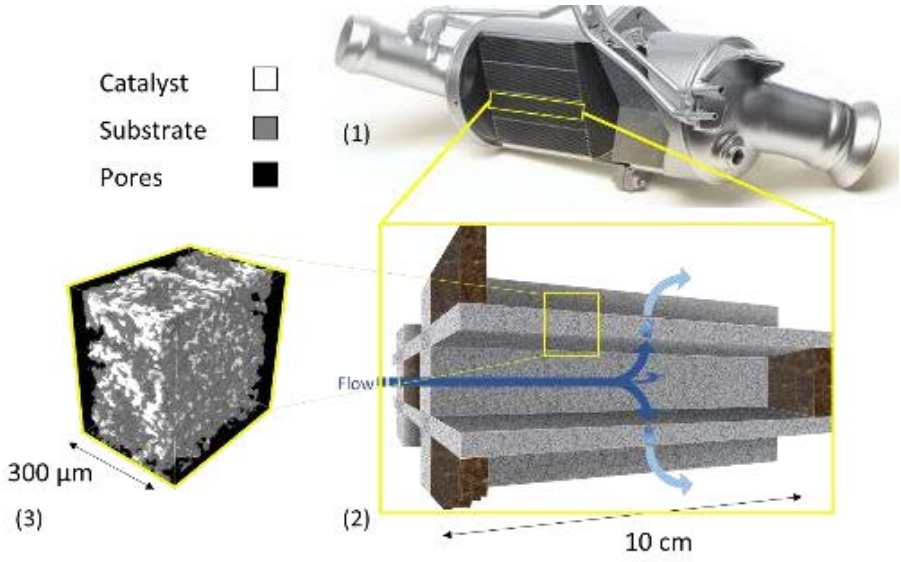

Figure 1: Illustration of the three scale levels of coated PF: (1) whole filter scale (~10 cm long), (2) channel scale (~1 mm wide), and (3) porous wall scale (~10 µm pore size).

Numerous studies have compared the effect of different substrates and/or amounts of coating on pressure drop, filtration efficiency and NO_X reduction of a SCR-DPF combination. A study on the performance of cordierite-based wall-flow filters coated with an SCR catalyst at different densities revealed that the impact of the catalyst coating on the pressure drop of the filter was negligible compared to the effect of soot accumulation (Rappé 2014). On the other hand, it was shown that variable catalyst coating amounts in different substrates can multiply the pressure drop through the wall up to 20 times compared to a bare filter (Swanson et al. 2013). In another study, various amounts of washcoat deposited on an SiC-based DPF were compared in terms of pressure drop and filter efficiency (Tsuneyoshi, Takagi, and Yamamoto 2011). The general conclusion was that higher catalyst coating amounts usually result in an increase in both filtration efficiency and pressure drop. In the case of gasoline particulate filters (GPF), a three-way catalyst (TWC) containing platinum group metals is usually used in the catalytic washcoat (Thomas et al. 2019). Studies similar to those on SCR-DPFs have been conducted on TWC-GPFs (Inoda et al. 2017; Lopez-Gonzalez et al. 2015; Richter et al. 2012), most of which concluded that, like SCR-DPFs,

washcoat deposition increases both the pressure drop and the capture efficiency. This can be explained by the loss of pore space caused by the deposition of the catalyst. Contrariwise, it has also been proposed that increased washcoat loadings can lead to decreased filter capture efficiency due to higher gas flow velocities and thus lower residence time (Joshi and Johnson 2018; Liu et al. 2018). A complete understanding of this issue is lacking in the literature and further work is needed to explain the impact of the amount of washcoat and its distribution in the pore space. Such an investigation would be very complex if conducted experimentally.

Therefore, in addition to experimental work, many studies have explored CPFs using numerical simulations. This approach has the advantage of being less costly, easier to manage, and less intrusive than bench experiments. Three different numerical PF modelling scales have been reported in the literature. Figure 1 illustrates the various PF scales usually modeled numerically. The largest is the whole filter scale. Models at this scale are, however, rarely used to predict the overall filtration performance of PFs except through semi-empirical or analytical expressions developed at smaller scales at which soot capture takes place. For more details on this modelling scale, the reader is referred to more exhaustive reviews (Konstandopoulos and Papaioannou 2008; Koltsakis et al. 2013). The middle scale refers to the channel scale, the modelling of which was pioneered by Bisset and Shadman (Bissett and Shadman 1985) and improved later by Watling et al. (Watling et al. 2017), among others. The related modelling and improvements have been reviewed in recent years (Koltsakis et al. 2013; Xuereb and Farrugia 2016), and usually consider 1D, 2D, or 1D+1D domains using a compartmental approach for the channel length and the wall thickness (Wurzenberger et al. 2016), and solving macroscopic conservation equations of mass, momentum, and energy in two adjacent channels of the PF. This modelling scale has the advantage of being simple and efficient for predicting back pressure and filter efficiency behaviour over time for well-characterized filters (Torregrosa et al. 2011; Gong et al. 2018). Filter cake evolution over driving cycles and time is often considered at this modelling scale (Bensaid et al. 2009; Lupše, Campolo, and Soldati 2016; Karamitros and Koltsakis 2017). The major drawback of this model, as with the largest scale, is that it is not able on its own to predict the impact of smaller-scale features of the porous wall medium on the performance of the filter. Indeed, in this approach, porous wall resistance to the flow is usually accounted for through the resolution of the Brinkman equations. For example, the prediction of the impact of washcoat distribution uniformity in the

porous wall on pressure drop and filtration efficiency is not possible without prior knowledge of small-scale structural properties such as permeability, tortuosity, and pore size distribution.

In recent years, advances in high-performance computing (HPC), improvements in computational memory and power, and the development of new imagery techniques such as tomography have made the numerical study of PF structures at the micron scale possible. They have also made it possible to represent the porous wall of the filter in greater detail. As such, considerable research interest has been directed toward porous media modelling. The review of Konstandopoulos et al. (Konstandopoulos, Kostoglou, and Vlachos 2006), one of the earliest studies, reported permeability predictions for two different washcoat distributions in the porous wall of an SiC-based DPF. The washcoat distribution was varied at the pore scale level by erasing washcoat voxels from a segmented scanning electron microscope (SEM) image using an unreported procedure. The results showed that a non-uniform distribution profile leads to higher permeability than a uniform one in the 0-30% range of pore volume filled with washcoat. However, neither the detailed characteristics of the two washcoat distributions nor their soot capture efficiency were reported by the authors, limiting the conclusions regarding the overall filtration performance of such washcoat depositions. More recently, an investigation of the impact of on-wall and in-wall depositions of catalyst on the filtration performance of the porous wall of an SCR-DPF reported better results with the on-wall deposition in terms of pressure drop, soot capture, and contact ratio between the deposited soot and the catalyst (Kong and Yamamoto 2018). However, the authors did not report any details with respect to the distribution uniformity of the in-wall deposited catalyst or the quantitative results of capture efficiency. Similarly, in the context of TWC-GPFs, other studies compared the filtration and catalyst performance of three cordierite filter structures with different in-wall and on-wall coating distributions (Tanaka, Miyoshi, and Sato 2018; Kočí et al. 2019) and reported that in-wall depositions were more permeable than mixed in- and on-wall depositions. Although these studies showed that detailed investigations of PF performance at the micron scale are feasible, a systematic parametric investigation of various coating distributions on filtration and catalytic performance was not done and capture efficiency was not considered. In all the aforementioned papers, the researchers employed a multi-step approach that appears to be well-suited for tackling PF modelling. First, a representative filter medium was generated using geometrical reconstructions such as spherical particle packing algorithms (Hayashi and Kubo 2008; Lee et al. 2018), simulated annealing (Matte-Deschênes et al. 2016), or real sample images from SEM images (Stewart et al.

2010) or computed tomography scans (Tsushima et al. 2010). Once the structure is reconstructed, computational fluid dynamics (CFD) methods such as the well-established finite volume method (FVM) (Kočí et al. 2019) or the well-suited lattice Boltzmann method (LBM) (Konstandopoulos, Kostoglou, and Vlachos 2006; Yamamoto et al. 2006; Stewart et al. 2010; Matte-Deschênes et al. 2016; Kong and Yamamoto 2018; Lee et al. 2018) can be employed to compute the flow field through the filter porous wall and thus calculate the medium permeability and/or the pressure drop. These CFD methods can also be used to retrieve other fields such as the temperature across the filter wall (Yamamoto and Nakamura 2011). Once the flow field has been computed, filter capture efficiency can also be obtained by tracking individual particle trajectories using Lagrangian approaches (Wiegmann, Rief, and Latz 2006; Vadeiko and Drolet 2009; Becker et al. 2016; Stewart et al. 2004) or solving mass transport equations using the Eulerian approach and using probabilistic models of soot deposition (Yamamoto and Ohori 2012; Tsushima et al. 2010). Physical phenomena at the micron scale can thus be studied using this multi-step methodology. However, to date, no study has been able to provide an overall and systematic understanding of the impact of the structural characteristics of catalytic washcoat deposition on both the filtration performance and the catalytic conversion of a CPF. To achieve this, a complete set of numerical models at the wall scale must be developed to predict the overall performance of a CPF. In particular, artificial washcoat deposition techniques must be developed to generate different catalyst coating distributions in the porous wall and predict its performance.

To pave the way for this ultimate goal, two specific objectives are pursued. The first is to develop modelling tools able to predict both the filtration and catalytic conversion performance of a catalyst-coated GPF at the microscopic scale. The second is to demonstrate the usefulness of these modelling tools by applying them to determine the most appropriate catalyst distribution profile in a cordierite porous wall of a GPF by comparing the performance of uniform and non-uniform washcoat distribution profiles. More specifically, the aim of the present investigation was to quantify the possible benefits of uniform catalyst deposition versus non-uniform deposition within the porous wall of the filter in terms of GPF performance. The present article focuses on filtration performance as defined by pressure drop and soot capture efficiency, while an upcoming companion paper will compare catalytic conversion performance (Belot et al. To be submitted (2020)). Soot and ash accumulation and the resulting filter clogging will be neglected here as a filter cake formation is less likely on the porous wall of GPFs due to lower soot concentrations,

soot oxidation by TWC and higher exhaust gas temperatures than in a DPF (Gong et al. 2018; Mikulic et al. 2010; Lambert et al. 2017) and because ash accumulation occurs mainly over extended use (Lambert et al. 2016; Joshi and Johnson 2018).

The remainder of the paper is organized as follows. In Section 2, the three-step numerical model developed in the present investigation and relying on the lattice Boltzmann method is examined in detail. In Section 3, the quality of the model predictions is assessed, and a detailed analysis of the impact of catalytic deposition uniformity on pressure drop, permeability, capture efficiency and, thus, overall filtration performance is presented. Lastly, Section 4 provides concluding remarks and the prospects of the present work for achieving the general objective of building a wall-scale model for predicting overall CPF performance.

2. THREE-STEP METHODOLOGY

To achieve the two specific objectives mentioned in the Introduction, the three-step methodology shown in Figure 2, which was partly inspired by the methodology proposed in (Matte-Deschênes et al. 2016), was developed and is presented in this section. It consists of (1) the numerical reconstruction of a representative elementary volume (REV) of the coated porous wall with various washcoat distributions (i.e., uniform and non-uniform) and coating amounts, generated using a novel set of erosion/dilation-based procedures, (2) the computation of the flow field using the lattice Boltzmann method (LBM) to obtain the back pressure (hereafter referred to as pressure drop or ΔP) across the wall, and (3) the calculation of soot particle trajectories by solving the Langevin equation to obtain the capture efficiency (E_f) of the porous wall. Knowing the ΔP and E_f of the reconstructed GPF wall, it is possible to compute the filter quality factor (Q_f), which is a criterion often used in air filtration by fibrous filters and employed here to compare the overall filtration performance of the different washcoat distributions within the porous wall. Here, the catalyst coating was assumed to be impermeable as its permeability (~10^{-15} m^2 according to (Kočí et al. 2019)) is at least two orders of magnitude lower than that of the resulting substrates studied and, therefore, its pore network was not resolved and thus accounted for.

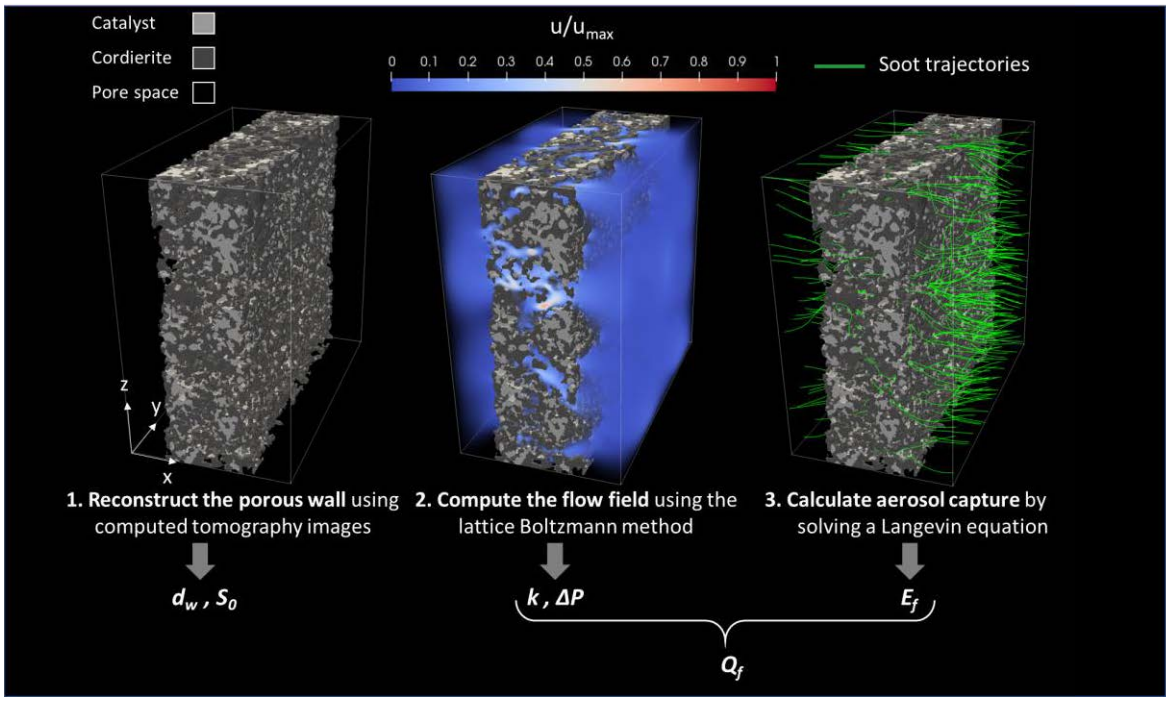

Figure 2: Illustration of the three numerical steps leading to the prediction of the filtration performance of a GPF porous wall at the microscopic scale.

2.1 Reconstruction and characterization of the porous wall

The first step in the development of a model able to predict the performance of a filter is the reconstruction of a piece of the porous wall that divides two adjacent channels of a coated GPF. The wall is composed of three phases: the pore space, the substrate (here cordierite), and the catalyst coating (also called washcoat). To generate a good numerical representation of the porous walls and their washcoat distribution profiles, multiple reconstruction methods can be considered. They all require different levels of information about the original base structure and the washcoat distribution profiles. One approach, the simulated annealing technique, uses stochastic algorithms (Matte-Deschênes et al. 2016). In this case, geometrical characteristics such as the phase correlation functions of a real substrate and coating deposition are needed but are not readily available. A second approach simulates the physical phenomena or processes involved in manufacturing catalyst-coated filters. The main drawback of this approach is that it can be very complicated and time consuming in the case of complex industrial processes. It also requires a great deal of

information about the manufacturing process itself, which is often not readily available. A good compromise and computationally efficient solution for achieving better precision and a more realistic reconstruction of the porous wall is to start from an actual numerical image of a coated GPF sample at the pore scale on which digital operations can be performed to reconstruct filter structures virtually. In the present study, an X-ray computed tomography (CT) image of a 3×3×1.5 mm^3 piece of a 1.16-mm wide channel of a cordierite-based GPF coated with a TWC washcoat was acquired using a General Electric *Phoenix Nanotom M*. The lab sample used, hereafter referred to as the original R&D sample (OS), was non-uniformly coated throughout the wall thickness, with 23.2% of the cordierite pore volume filled with washcoat. A stack of 256 images, each composed of 801×779 pixels representing a section of the porous wall, was extracted from the 3D raw image of the OS sample. This stack of images was then reconstructed into a 3D image, as shown in Figure 3. The voxel resolution in every direction was $dx = 1.246\ \mu m$. The raw data were encoded using an 8-bit grey scale, and the image was segmented into pore space, cordierite, and catalyst phases based on a thresholding algorithm (Greiner et al. 2019).

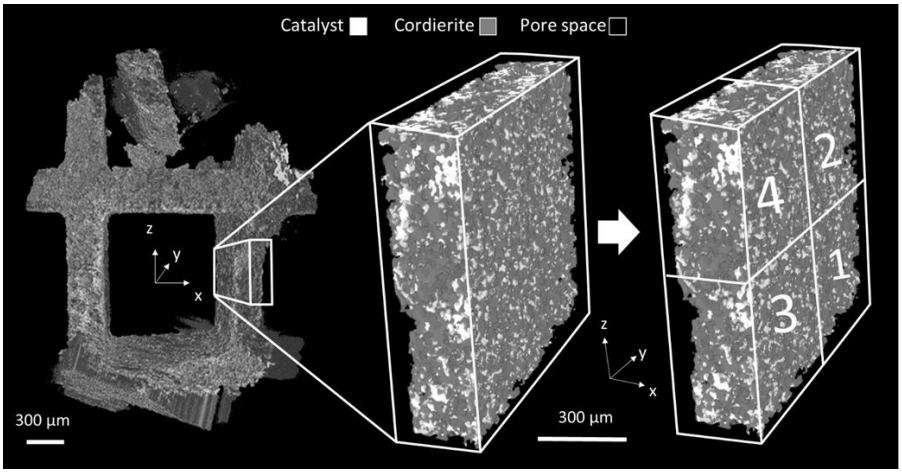

Figure 3: Representation of the 3D image of a section of the porous wall (middle) extracted from the raw data of a channel piece from the OS sample of a specially prepared TWC-GPF (left), and the later splitting of this wall section into subdomains used for the computations (right).

Once the wall section was segmented, a novel artificial washcoat deposition method applied to the resulting three-phase image and relying on classical morphological dilation and erosion algorithms used in image analysis (Young 1983) was devised to modify the original washcoat distribution

profile. This method is based on a set of three independent procedures depending on the type of washcoat distribution profiles to be reconstructed, which are illustrated using 2D slices in Figure 4. The first procedure of the artificial deposition method created a uniform distribution profile, i.e., completely different from the non-uniform distribution profile of the OS sample. To obtain a uniform distribution profile, the original coating deposition (white pixels in Figure 4) was digitally erased and was replaced by pore space pixels. Next, the substrate (grey pixels in Figure 4) was dilated from its surface using a sphere of a specific diameter as a 3D structuring element by means of a custom-written MATLAB program based on the MATLAB Central File Exchange routine STREL3D (version 1.1.0.0) (Xie 2014). The added voxels resulting from this morphological dilation of the substrate were converted into washcoat voxels (white pixels in Figure 4), creating a uniform washcoat deposition within the porous wall, the coating amount of which was determined by the size of the sphere used as a structuring element. Here, the sphere diameters used varied from 2 to 9 times the voxel size.

The second and third procedures of the artificial deposition method aimed at creating non-uniform distribution profiles that follow from the OS sample non-uniformity and differ depending on whether the amount of washcoat is larger or smaller than that of the OS sample. Specifically, the two procedures were devised to either (1) increase the coating amount of the OS sample while accentuating its non-uniformity using a dilation-based technique, or (2) decrease the coating amount of the OS sample while decreasing its non-uniformity using an erosion-based technique. To increase the coating amount, the catalyst phase was dilated using spherical structuring elements of increasing diameter (from 2 to 9 times the voxel size) as previously described for the uniform coating profile creation procedure. Note that the dilation procedure only takes place within the pore space and not the substrate. To decrease the coating amount, the procedure was slightly more complex and is detailed in the insert of Figure 4. The substrate phase was first merged with the original catalyst phase to form a solid phase (white pixels in frame (b) of the insert in Figure 4). The new solid phase was then eroded using a spherical structuring element of a specific diameter (from 2 to 9 times the voxel size), with higher diameters resulting in lower coating amounts. Lastly, the original substrate phase was overlaid on the resulting catalyst and pore phases as shown in Figure 4. This technique prevented the creation of gaps between the catalyst and substrate phases that occur when a direct erosion of the original catalyst phase is performed.

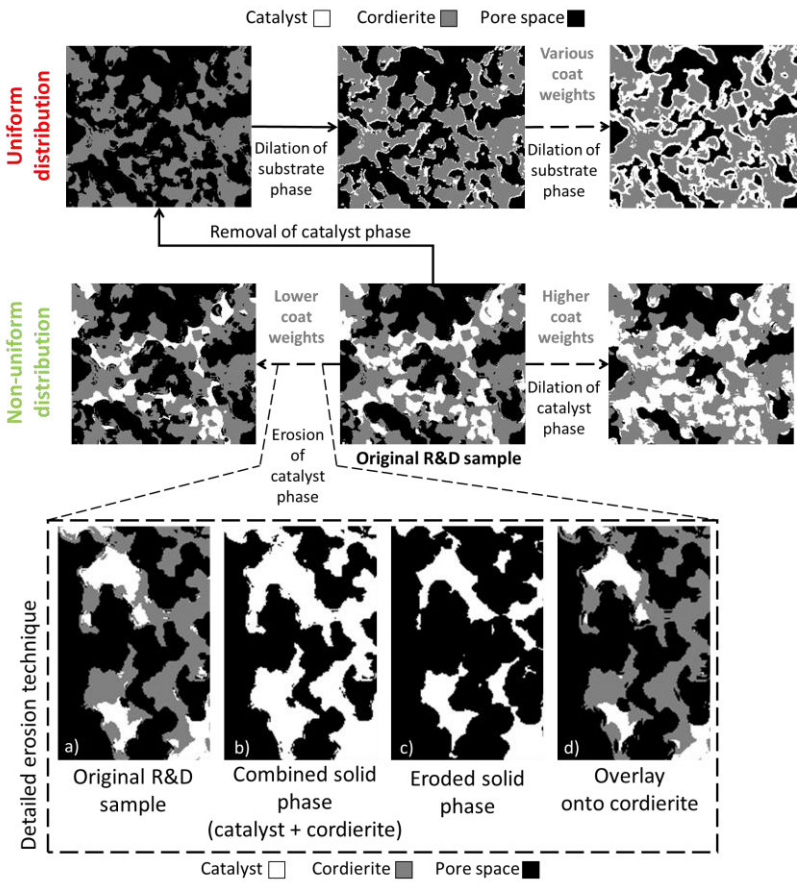

Figure 4: 2D illustrations of the different deposition procedures used to obtain the uniform and non-uniform distribution profiles from the OS sample image. The insert at the bottom illustrates the more complex erosion technique employed to obtain a thinner non-uniform catalyst deposition from the OS sample distribution profile.

Following these two procedures, four and eight structures of increasing coating amount with, respectively, uniform and non-uniform washcoat distribution profiles (hereafter denoted as U1 to U4 and N1 to N8, respectively) were created. In addition to these 12 structures, two other structures were considered: (1) the OS sample, which can be considered as part of the non-uniform structure series, and (2) the bare wall (BW) structure (i.e., the OS structure from which the catalyst phase was completely removed), which can be considered as a limiting case with the coating amount equal to zero for both the uniform and non-uniform structure series. This brought the total number of structures studied to 14. The dimensions of all the structures were 256×801×779 voxels at the tomographic image resolution (i.e., $dx = 1.246\ \mu m$). For ease of computation, each of these

structures was split into four 256×400×389-voxel subdomains, as shown in Figure 3, resulting in a total of 56 structures. The accuracy of the permeability predictions with respect to the subdomain size chosen is assessed in detail in Appendix A.

Once reconstructed, the characterization of the porous structures is an essential step for an in-depth understanding of the difference in filtration performance between the two washcoat distribution profiles. The most obvious metrics is the volume fraction of the pore space (i.e., the porosity), denoted as ε, defined as:

$$\varepsilon = \frac{V_{por}}{V_{tot}} \tag{1}$$

where V_{por} is the volume of the pore space and V_{tot} is the total volume of the porous medium. This value can be calculated by dividing the number of pore voxels by the total number of voxels. Knowing the porosity of the reconstructed structures, the fraction of pore volume filled with catalyst can be calculated as:

$$f_w = 1 - \frac{\varepsilon}{\varepsilon_{BW}} \tag{2}$$

where ε_{BW} is the porosity of the bare wall. The specific surface area S_0 is another important characteristic of a porous medium as it is strongly related to permeability and capture efficiency, as we shall see later, and is linked to the interfacial area S between the two phases per unit volume of the solid phase through:

$$S_0 = \frac{S}{(1-\varepsilon)V_{tot}} \tag{3}$$

Here, the specific surface area of each digitized structure was calculated using the PoroDict® module of the commercial software GeoDict® (version 2018, Math2Market GmbH, www.geodict.com) using a statistical method (Ohser and Mücklich 2000). Both ε and S_0 can be used to evaluate the mean pore diameter d_w of the wall given by:

$$d_w = \frac{2\varepsilon}{3(1-\varepsilon)}\frac{6}{S_0} \tag{4}$$

Lastly, pore size distribution is a sensitive metric for characterizing the pore space and for differentiating one porous medium from another. Although there is no strict and unambiguous definition of a pore, many methods exist in the literature to evaluate this characteristic function. In the present study, the PoroDict® module of the commercial software GeoDict® was used to compute the pore size distribution of the reconstructed structures based on a granulometry technique (Soille 1999). Additional statistical structural descriptors, namely the two-point probability function and the lineal path, are also provided in Appendix B. They may help reconstruct these structures using the simulated annealing technique (Matte-Deschênes et al. 2016), for instance, to enable future use of these structures by any interested reader.

2.2 Computation of the flow field through the porous wall

The second step in the development of a model able to predict filter performance is the calculation of the flow field through the porous wall. Although several other CFD methods (particularly Explicit-Jump, SIMPLE-FFT, and LIR methods as well as the FVM) implemented in commercial or open-source software packages (such as GeoDict® ("GeoDict" 2018) or OpenFOAM® ("OpenFOAM")) could also have been well suited in this context (Azimian, Cheng, and Wiegmann 2017; Kočí et al. 2019), the lattice Boltzmann method (LBM) was here chosen as it is particularly effective for porous media due to the several reasons: (1) its ease in dealing with complex geometries and the associated mesh generation (Vidal et al. 2009), (2) its parallel efficiency on large-scale parallel and distributed computer systems due to the inherent locality of its explicit scheme (Vidal, Roy, and Bertrand 2010a, 2010b), (3) its relative simplicity of implementation, and (4) its capability to solve partial differential equations, making an LBM scheme a generic partial differential equation solver for porous media (Krüger et al. 2017b). Furthermore, although the present study only required steady state flow computations, the LBM is an intrinsically transient solver (as opposed to current GeoDict® flow solvers using Explicit-Jump, SIMPLE-FFT, and LIR methods), a feature which will be used in future studies related to the present investigation. We did, however, use the SIMPLE-FFT GeoDict® flow solver to assess the quality of the LBM code predictions for steady state flows.

Assuming an isothermal incompressible flow, the LBM does not tackle the problem at a continuum mechanics scale, which would require solving the incompressible Navier-Stokes equations as classical CFD methods do, but rather at a mesoscopic scale using statistical mechanics following

the Boltzmann equation in which the probability distribution function is discretized in the time, space, and velocity domains using a set of microscopic velocities (Krüger et al. 2017b). The LBM scheme has been shown to satisfactorily recover the transient Navier-Stokes equations for incompressible flows in the limits of lower Mach and Knudsen numbers (Krüger et al. 2017b). In this work, a D3Q15 velocity set and a single-unit dimensionless relaxation time were here used for the sake of computational and memory usage efficiencies, as explained in (Vidal, Roy, and Bertrand 2010b).

The LBM code developed in (Vidal, Roy, and Bertrand 2010a, 2010b) was used to calculate the flow velocity field of each of the 56 reconstructed media and the reader is referred to these papers for more details about the LBM and its implementation. No mesh generation was needed for these calculations as the LBM scheme uses directly the voxelization of the reconstructed geometries as a computational grid or lattice, with a lattice spacing being equal to the CT image resolution, i.e., $dx = 1.246\ \mu m$. The LBM implementation only retains the pore voxels and, as such, probability distribution functions arriving at a wall (solid voxel) are bounced back to the pore space using the half-way bounce back boundary condition (Vidal, Roy, and Bertrand 2010a). The flow here is driven by a pressure drop implemented through an added body force in the discretized Boltzmann equations in the flow direction (here the wall thickness, i.e., x direction) at each lattice site and each time step (see (Bertrand et al. 2012) or (Krüger et al. 2017b), for detailed implementations). The outside domain boundary conditions used in these simulations were periodic for the probability distribution functions in the direction of the flow (x) and symmetric in the directions perpendicular to the flow (y,z). Lastly, two buffers of 100 fluid voxels were added upstream and downstream from the structures to prevent too large edge effects and facilitate the implementation of the periodic flow boundary condition. The size of the buffer zones can influence the uniformity of the velocity profiles at the inlet and outlet, but their influence on the permeability has been evaluated to be much lower than 1% at the size selected here. The effective dimensions of the 56 structures studied were thus 456×400×389 voxels. It must be mentioned that even if the flow was driven by a pressure drop, and as long as the flow regime remained laminar, the resulting velocity field could be linearly rescaled afterward such that the targeted superficial velocity U was obtained and ΔP was corrected accordingly as a result. The physical parameters used for these LBM calculations of gas flow through the 56 porous structures studied are summarized in Table 1, in which it is assumed that the exhaust gases have the same properties as air.

Table 1: Physical parameters used for flow field calculations with the LBM.

Parameter	**Symbol**	**Value**
Fluid density ($kg.m^{-3}$)	ρ	0.543
Fluid dynamic viscosity ($kg.m^{-1}.s^{-1}$)	μ	3.18×10^{-5}
Superficial velocity ($m.s^{-1}$)	U	0.055
Temperature (K)	T	650

Once the velocity field was obtained using the LBM for each of the 56 structures and ΔP was calculated, it was possible to retrieve a key macroscopic property of the porous medium, i.e., which is the hydraulic Darcy's permeability using Darcy's law for laminar flows (Dullien 1979) given by:

$$k_D = -\frac{\mu U L}{\Delta P} \tag{5}$$

where L is the wall thickness. This physical property is a material characteristic when calculated using pore-based Reynolds numbers lower than 10. In the present study, the pore-based Reynolds number Re_p lay in the laminar Darcy's regime for all the conditions investigated (Bird, Stewart, and Lightfoot 2007):

$$0.03 \leq Re_p = \frac{\rho U d_c}{\mu(1-\varepsilon)} \leq 0.3 < 10 \tag{6}$$

where d_c is the diameter of the spherical collectors constituting a packed bed having the same specific surface area as the PF wall and is defined by (Dullien 1979):

$$d_c = \frac{3(1-\varepsilon)}{2\varepsilon} d_w = \frac{6}{S_0} \tag{7}$$

For accuracy assessment purposes and despite being more appropriate for packed beds of spherical particles, the computed permeability was compared to the Blake-Kozeny (BK) correlation (Blake 1922; Kozeny 1927) given by:

$$k_{BK} = \frac{1}{4.1\bar{6}\,{S_0}^2}\frac{\varepsilon^3}{(1-\varepsilon)^2} \tag{8}$$

Lastly, note that while the ΔP and k_D of the 56 reconstructed structures were computed using our own LBM code, the same calculations could have been performed with the FlowDict® module of the commercial software GeoDict® as these calculations only require steady state solutions. However, as already mentioned, the LBM makes efficient parallelization possible on massively parallel computer clusters. Because of this, launching the simulations on dedicated computer clusters on several tens of cores resulted in very short computational times, i.e., in the order of minutes (see Section 3.2.1). Moreover, the LBM solved the transient flows through the structures, which provided additional information on flow behaviour through the structures over time that could be used in later analyses. Nevertheless, the initial LBM calculations within the OS structure were assessed using calculations made with the SIMPLE-FFT solver of FlowDict® and with predictions from the Blake-Kozeny equation (see Section 3.2.1).

2.3 Computation of soot particle trajectories in the porous wall

The last step in the development of a model able to predict the behaviour of filter performance is the calculation of the soot capture efficiency of the porous wall of a GPF. Two modes of filtration occur in a PF. The first is deep-bed filtration when the filter is still clean and the particles can penetrate deeply into the porous walls. Over time, ash/soot can accumulate and form a soot cake layer at the inlet surface of the channel wall. Clean filter capture efficiency was calculated using the FilterDict® module of GeoDict®. The approach consists of launching a large number of soot particles, represented by spheres with equivalent mobility diameters (Thomas et al. 2017), into the flow passing through the 56 previously reconstructed structures. For each particle diameter under investigation (with $d_p(\mu m) \in \{1.00, 0.500, 0.375, 0.325, 0.275, 0.225, 0.175, 0.125, 0.090, 0.03\}$), 25000 particles were launched from locations evenly distributed on the domain entry plane. Soot capture efficiency was then calculated for a given particle size as given by:

$$E_f = \frac{N_{in} - N_{out}}{N_{in}} \tag{9}$$

where N_{in} and N_{out} are, respectively, the number of particles launched at the inlet and the number collected at the outlet of the filter. In the packed bed model, the filter efficiency for a specific particle size can be linked to the efficiency of a single collector through the single collector theory as given by (Lee and Gieseke 1979):

$$E_f = 1 - P_p = 1 - e^{-\beta\,\eta(1-\varepsilon)L} \tag{10}$$

where P_p is the particle penetration, η is the single collector efficiency, L is the thickness of the filter, and β is a constant or a function of porosity linked to the surface area of the collector for which many approximate expressions exist that are either derived analytically or obtained empirically (e.g., $\beta = \frac{4}{\pi d_c \varepsilon}$ for fibrous filters (Lee and Liu 1981) or $\beta = \frac{3}{2\varepsilon d_c}$ for spherical pack beds (Konstandopoulos 2000)). As larger soot particles are made of dendritic clusters of smaller primary particles, the density of the soot particles is a function of their diameter, which was chosen based on the diameter reported in (Keskinen et al. 1998), and is given by:

$$\rho_p = 1550 - (1550 - 155)\left(1 - \exp\left(-6.908\left(\frac{\log(0.03) - \log\left(10^6 \times d_p\right) -}{\log(0.03)}\right)^{4.28}\right)\right) \tag{11}$$

where d_p is the soot particle mobility diameter. A Lagrangian method was then used to follow each particle trajectory independently throughout the filter. To do so, Newton's second law of motion is solved for each particle considering the drag force and a stochastic term representing Brownian diffusion. This term is calculated using the diffusion coefficient of soot particles $D = \frac{k_B T}{\gamma}$ (where k_B is the Boltzmann constant and $\gamma = 6\pi\mu\frac{d_p}{2C_c}$ is the friction coefficient of a spherical particle in Stokes flow), and a 3D Wiener process $\boldsymbol{w}$ for a Brownian diffusion force in a way similar to that in (Vadeiko and Drolet 2009). Adding this term gives the following Langevin equation:

$$\frac{d\boldsymbol{v}(t)}{dt} = \frac{3\pi\mu d_p}{mC_c}\left(\boldsymbol{u}(\boldsymbol{x}) - \boldsymbol{v}(t) + \sqrt{2D}\frac{d\boldsymbol{w}(t)}{dt}\right)$$
$$\frac{d\boldsymbol{r}(t)}{dt} = \boldsymbol{v}(t) \tag{12}$$

where $\boldsymbol{r}$ and $\boldsymbol{v}$ are, respectively, the position and velocity of the particle, $\boldsymbol{u}$ is the previously obtained flow velocity, μ is the dynamic viscosity of the fluid, d_p is the equivalent soot diameter of the particle, m is the mass of the particle, and C_c is the Cunningham correction factor given by (Thomas et al. 2017):

$$C_c = 1 + A\,Kn + B\,Kn\,\exp\left(\frac{-C}{Kn}\right) \tag{13}$$

where $A \approx 1.17$, $B \approx 0.525$, and $C \approx 0.78$ are empirical parameters given in (Crowe 2005). Kn is the particle Knudsen number given by:

$$Kn = \frac{2\lambda}{d_p} \tag{14}$$

where λ is the mean free path of the fluid molecules. Other forces such as electrostatic attraction, thermophoresis, or gravity could have been considered but were excluded here because of their insignificant impact (Hinds 1999; Matte-Deschênes et al. 2016). A one-way coupling between the calculated flow field and the Langevin equation was considered in this work because the soot concentration was low and the flow disturbance caused by the motion of soot particles could be overlooked. This calculation takes into account three main particle capture mechanisms, namely Brownian diffusion, interception, and inertial impaction (Hinds 1999). The addition of these three capture mechanisms results in a capture efficiency relationship as a function of particle size that is typically shaped like a "smile", as reported in the literature for GPF and for fibrous filters (Joshi and Johnson 2018; Gervais et al. 2015). If a soot size distribution would be available, a composite capture efficiency could be calculated from this capture efficiency relationship, but soot coalescence/breakage cannot be account for in the current model. The soot diameter for which the capture efficiency is the lowest is usually taken as a reference value known as the capture efficiency of the most penetrating particle size (or MPPS). In the context of GPF, this diameter is usually

around 200-300 nm (Joshi and Johnson 2018). Therefore, the range of soot diameters tested in the present study was mainly centred on this range, which is actually close to the upper limit of soot size encountered in GPFs (Graves, Koch, and Olfert 2017). A particle was considered captured when the distance between its centre and an inner wall surface voxel was smaller than its radius. Once captured, it was assumed that the particles stick to the solid wall due to short-range electrostatic forces and cannot be reentrained by the flow. This approximation is valid for low particle Reynolds numbers (Hinds 1999), which is the case here:

$$8 \times 10^{-5} \leq Re = \frac{\rho U d_p}{\mu} \leq 3 \times 10^{-4} \ll 1 \tag{15}$$

2.4 Calculation of the porous wall quality factor

Knowing the ΔP and E_f values of a PF, it is possible to calculate a filter quality factor (Q_f) (sometimes also called a figure of merit) that is a relevant criterion for judging the overall filtration performance of a porous medium and that has been more commonly employed in the field of fibrous filters. The Q_f is defined as (Hinds 1999):

$$Qf = \frac{-log\,(1 - E_f)}{\Delta P} \tag{16}$$

The main advantage of this metric is that it is independent of the wall thickness that can be regarded as the filtration performance achieved with respect to the energy input into the system.

3. RESULTS AND DISCUSSION

The presentation of the results is divided into four parts. First, the 56 numerical structures reconstructed for the present investigation are characterized using the statistical and global structural descriptors described in Section 2. Then, the flow properties of the various porous walls predicted by the LBM are given and compared with predictions from the correlation mentioned in Section 2. Next, the results of filtration efficiency obtained by the resolution of the Langevin equation are presented and analyzed in detail. Lastly, the filter quality factor is calculated for every structure to compare the filtration performance of uniform and non-uniform deposition profiles at different coating amounts. The advantage of a uniform deposition profile compared to a non-uniform deposition profile is then assessed.

3.1 Characterization of the reconstructed structures

Once the 56 porous walls with varying amounts of washcoat and degrees of uniformity were numerically reconstructed, the global and statistical structural descriptors described in Section 2 could be calculated to characterize the structures. The porosities and the corresponding fractions of pore volume filled with catalyst (i.e. f_w calculated using Eq. (2)) for all the structures studied in the present investigation are presented in Table 2 and Table 3, respectively, for the non-uniform and uniform washcoat distribution profiles.

Table 2: Porosity values (ε) and corresponding fractions of pore volume filled (f_w) by the catalyst for all reconstructed non-uniform washcoat distribution profiles.

Sample ID:	**BW**	**N1**	**N2**	**N3**	**OS**	**N4**	**N5**	**N6**	**N7**	**N8**
Section	**Porosity (%)**									
1	68.3	60.4	58.6	56.1	54.6	52.0	48.8	46.4	42.7	36.7
2	67.2	58.3	56.3	53.7	52.2	49.5	46.4	44.0	40.3	34.6
3	69.8	60.6	58.6	55.8	54.2	51.5	48.1	45.7	41.9	36.0
4	67.8	55.4	53.1	50.2	48.5	45.7	42.3	39.9	36.2	30.7
Average	68.3	58.7	56.7	54.0	52.4	49.7	46.4	44.0	40.3	34.5
	Pore volume filled with washcoat (%)									
Average	0.0	14.0	17.0	20.9	23.2	27.2	32.0	35.6	41.0	49.4

[a] BW: bare wall without washcoat, OS: original R&D sample, N: reconstructed non-uniform washcoat distribution profiles

Table 3: Porosity values (ε) and corresponding fractions of pore volume filled (f_w) by the catalyst for all reconstructed uniform washcoat distribution profiles.

Sample ID:	**BW**	**U1**	**U2**	**U3**	**U4**
Section	**Porosity (%)**				
1	68.3	59.4	50.5	39.9	33.0
2	67.2	57.7	48.6	38.0	31.2
3	69.8	61.1	52.4	42.0	35.2
4	67.8	58.4	49.2	38.4	31.4
Average	68.3	59.2	50.2	39.6	32.7
	Pore volume filled with washcoat (%)				
Average	0.0	13.3	26.4	42.0	52.1

[a] BW: bare wall without washcoat, U: reconstructed uniform washcoat distribution profiles

In addition to porosity, another very important global descriptor for porous media revealed by the Blake-Kozeny correlation (see Eq. (8)) is the specific surface area S_0 defined in Eq. (3). The specific surface area decreases when the catalyst coating amount increases for both the uniform and non-uniform washcoat distribution profiles as shown in Figure 5. In addition, the specific surface area decreases more rapidly for a structure with a non-uniform washcoat distribution profile than for one with a uniform washcoat distribution profile for the same amount of washcoat. As expected, this trend suggests that small pore channels are more impacted as the pore space is filled with a non-uniform distribution than with a uniform one, since they usually contribute much more to the specific surface area. Knowing the specific surface area and the porosity, the mean pore diameter could be evaluated using Eq. (4), as shown in Figure 6. A gradual decrease in the mean pore diameter is observed as the coating amount increases for a uniform distribution profile since adding more catalyst over the entire substrate tends to uniformly reduce the pore sections. On the other hand, the behaviour of the mean pore diameter as the coating amount increases for the non-uniform distribution profile is non-linear and non-intuitive. The mean pore diameter reaches a maximum when $f_w \leq$ ~30%. This can be explained by the fact that non-uniform filling of the pore volume closes the small pores first, which corroborates the findings for the specific surface area. As a result, the larger pores make a greater contribution to the mean value of the remaining pores, and the mean pore size increases up to a certain filling degree, after which the remaining large pores are gradually filled, leading to a gradual decrease in the mean pore size. The pore size distributions plotted in Figure 7 clearly confirm this explanation by showing that when $f_w \leq$ ~30%,

only the small pores (i.e., those with diameters smaller than 20 μm) of the non-uniform profiles are impacted. On the other hand, all pore sizes are affected to a similar extent by the addition of washcoat in the case of the uniform profiles.

The structural properties of some of the virtual porous walls generated, particularly the non-uniform ones, thus behave non-linearly as the pore space is filled. This suggests that nonintuitive effects on ΔP and E_f may result from these characteristics. We shall return to this when we describe how filtration performance is affected by the addition of uniformly or non-uniformly distributed washcoat.

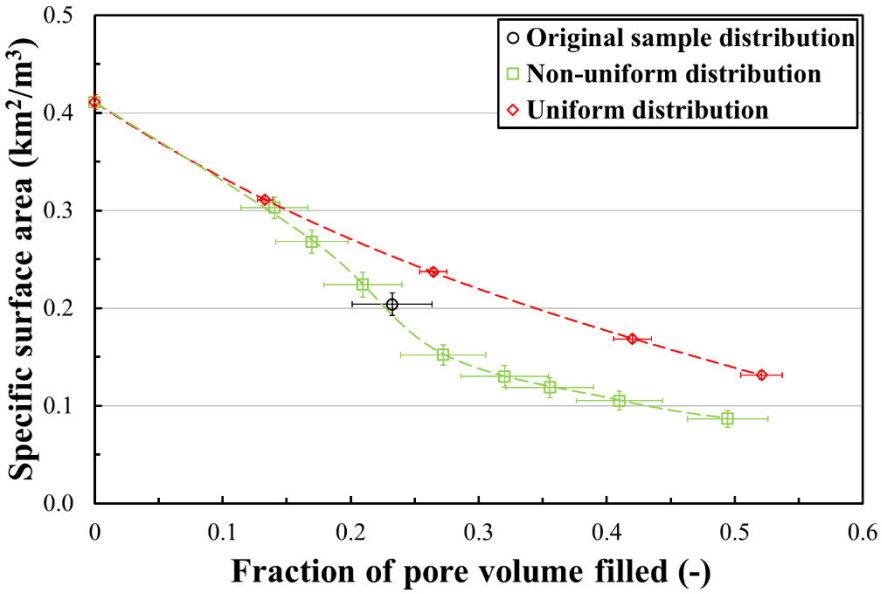

Figure 5: Comparison of specific surface areas (S_0) of the digitized structures as a function of the amount of washcoat (f_w) for the two washcoat distribution profiles, for all the reconstructed GPF porous wall structures. The dashed lines are a guide for the eye, and the error bars represent the standard deviations of the reported mean values for the four wall subdomains.

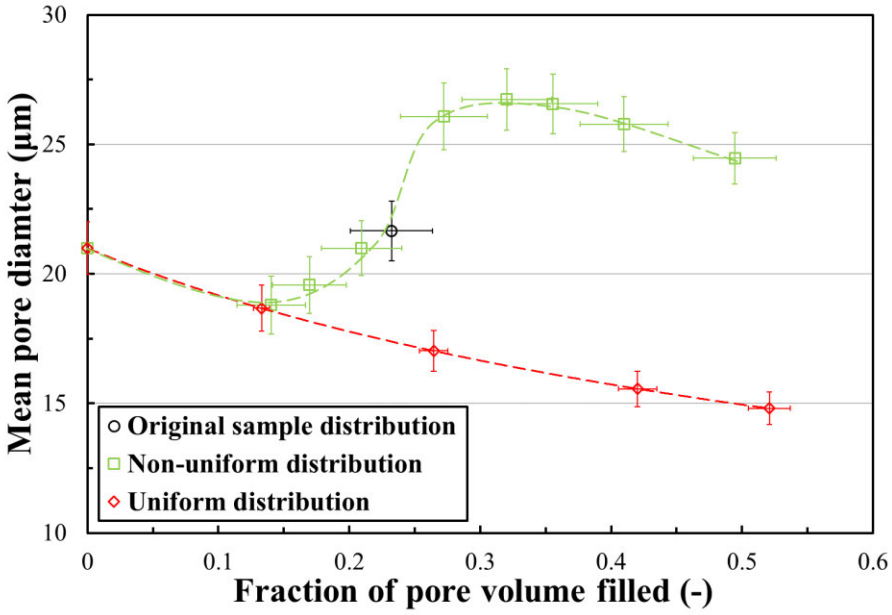

Figure 6: Comparison of mean pore diameters (d_w) as a function of the amount of washcoat (f_w) for the two washcoat distribution profiles, for all the reconstructed GPF porous wall structures. The dashed lines are a guide for the eye, and the error bars represent the standard deviations of the reported mean values for the four wall subdomains.

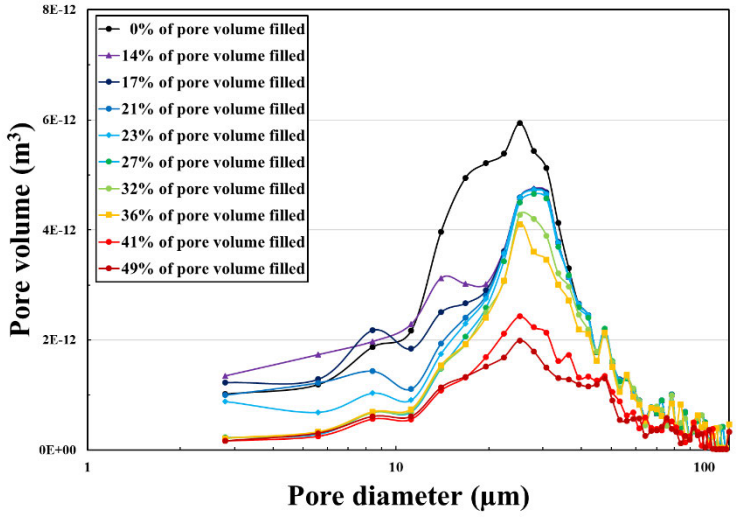

(a)

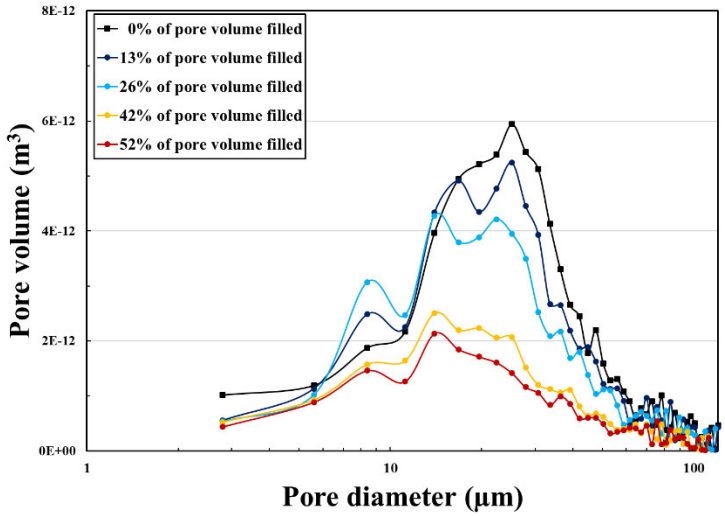

(b)

Figure 7: Comparison of pore size distributions calculated by the granulometry technique (using GeoDict®, (Soille 1999)) for a (a) non-uniform and (b) uniform washcoat distribution profiles in Subdomain 1 of the reconstructed GPF porous wall structures.

For the sake of completeness, we also provide in Appendix B two other statistical structural descriptors, namely the two-point probability and the lineal-path functions, for the two series of distribution profiles and all coating amounts.

3.2 Gas flows through the reconstructed structures

In this section, the accuracy and performance of the LBM code used to compute the flow field in the OS sample is first assessed. Then, the impact of various washcoat distribution profiles on the flow properties of the reconstructed porous walls is examined in detail.

3.2.1 Model assessment and computational performance

To assess the computations of the flow field through the reconstructed structures using the LBM code, the permeability of the four sections of the OS sample were compared to the results obtained with the FlowDict® module of the GeoDict® software using the SIMPLE-FFT Stokes solver and the predictions from the Blake-Kozeny correlation (i.e., Eq. (8)). The results are shown in Figure 8.

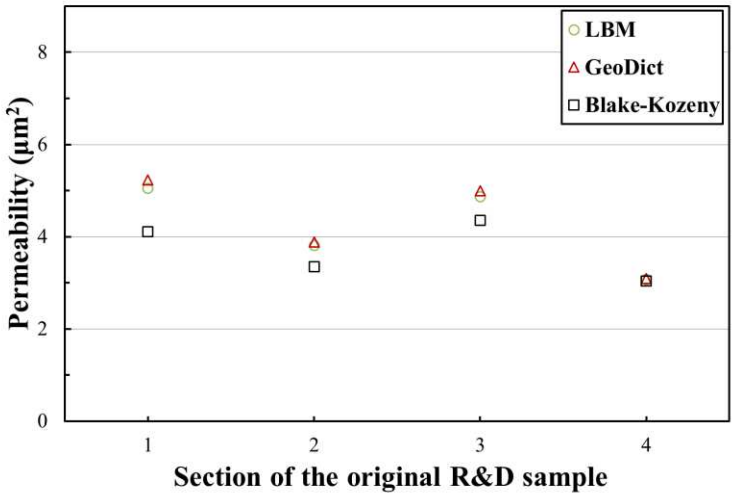

Figure 8: Comparison of permeability predictions by the LBM code, GeoDict® software, and the Blake-Kozeny correlation for the four subdomains (Figure 3) of the OS sample.

Keeping in mind that permeability is an extremely sensitive material property, there is good agreement between the different methods. The LBM code and GeoDict® give very similar permeability results, which lead to slightly higher permeability values than the predictions from the Blake-Kozeny correlation for three of the four porous wall subdomains analyzed. A detailed validation study of the LBM predictions reported here is provided in (Belot et al. To be published (2020)).

The computational time of our LBM code for a 456×400×389-voxel porous wall subdomain was approximately 6 hours on 8 cores (2.67 GHz Intel Xeon X5650 Westmere processor). The simulations used approximately 3.5 GB of RAM. As permeability calculations only require steady state flow fields and as the LBM is intrinsically a transient flow solver, GeoDict® steady state flow solvers are efficient alternatives to the LBM in this context as the computational time of the SIMPLE-FFT Stokes solver was approximately 12 hours on 2 cores (2.5 GHz Intel Xeon E5-2430V2 processor) and used only 0.8 GB of RAM. However, the LBM code has effective distributed parallelization capabilities that allow it to tackle very large domains in a reasonable computational time. For example, Figure 9 presents the steady state flow field computed by the LBM code on the whole OS sample. The CPU time was only 2 hours on 100 cores for the 456×801×779-voxel domain size. It was not possible, however, to evaluate the parallel capabilities

of GeoDict® because of the limitations of our license. The LBM code was used for the reminder of the study.

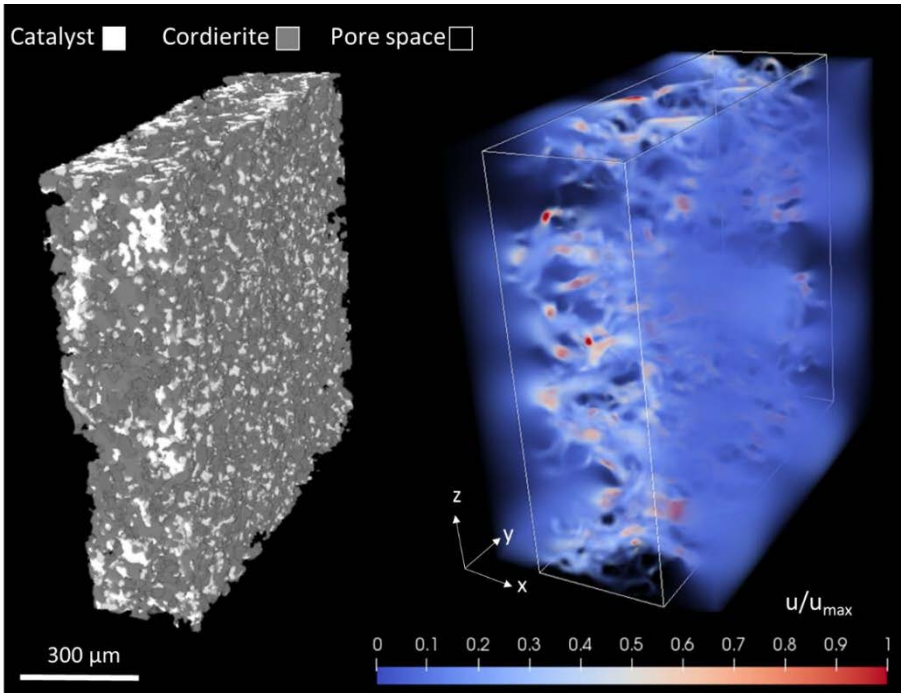

Figure 9: Structure (left) and flow field (right) in the original 456×801×779-voxel OS sample computed with the LBM code. The color scale represents the normalized gas velocity.

3.2.2 Permeability predictions

Having assessed the quality of our flow computations using the LBM code, we next explored the impact of the washcoat distribution profiles on permeability and pressure drop using the 56 structures characterized in Section 3.1. The average permeabilities of the four wall subdomains are plotted in Figure 10 for the uniform and non-uniform distribution profiles at the various coating amounts investigated.

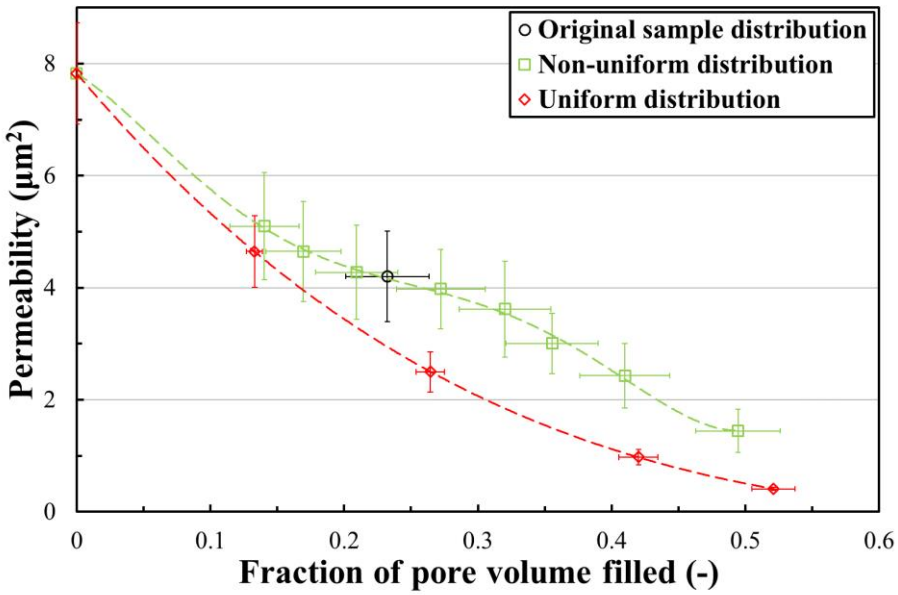

Figure 10: Comparison of the permeabilities (k) predicted by the LBM-based numerical model as a function of the amount of washcoat (f_w) for the two washcoat distribution profiles in the reconstructed GPF porous wall structures. The dashed lines are a guide for the eye, and the error bars represent the standard deviations of the reported mean values for the four wall subdomains.

As the pore volume was filled with an increasing amount of washcoat, the permeability decreases for both the uniform and the non-uniform distribution profiles, as expected. The addition of catalyst is detrimental to the gas flow, but this is to the benefit of better noxious gas conversions, which will be evaluated in a future work. A quadratic decrease in permeability as a function of the pore volume filled by the catalyst is found for the uniform distribution profile, whereas the decrease is less pronounced but more non-linear for the non-uniform distribution profile. The relative difference in permeability between the uniform and non-uniform catalyst profiles is up to 125% when $f_w \approx 50\%$. In the case of the uniform distribution, all flow pathways in the porous wall are affected by an increasing amount of washcoat so that they all narrowed to a similar extent. In the case of the non-uniform distribution, the relation between pore volume filled with catalyst and mean pore diameter is not linear, as seen in Figure 6. Initially, as more and more catalyst is added to the pore space, the small pores are plugged preferentially, as seen in Figure 7(a), leaving more big pores and preferential pathways untouched such that the permeability is less affected by an

increasing amount of catalyst. Interestingly, the trend for the non-uniform distribution profiles exhibited an inflection point near the OS data point (black open circle in Figure 10). In Appendix C, a comparison is made between the permeability predictions obtained in the present study and the ones from (Konstandopoulos, Kostoglou, and Vlachos 2006), showing that both the substrate and the type of washcoat non-uniformity can lead to somewhat different impacts on permeability.

3.2.3 Pressure drop predictions

For the sake of completeness and because it is of more practical use than permeability, Figure 11 presents the pressure drops through the reconstructed structures.

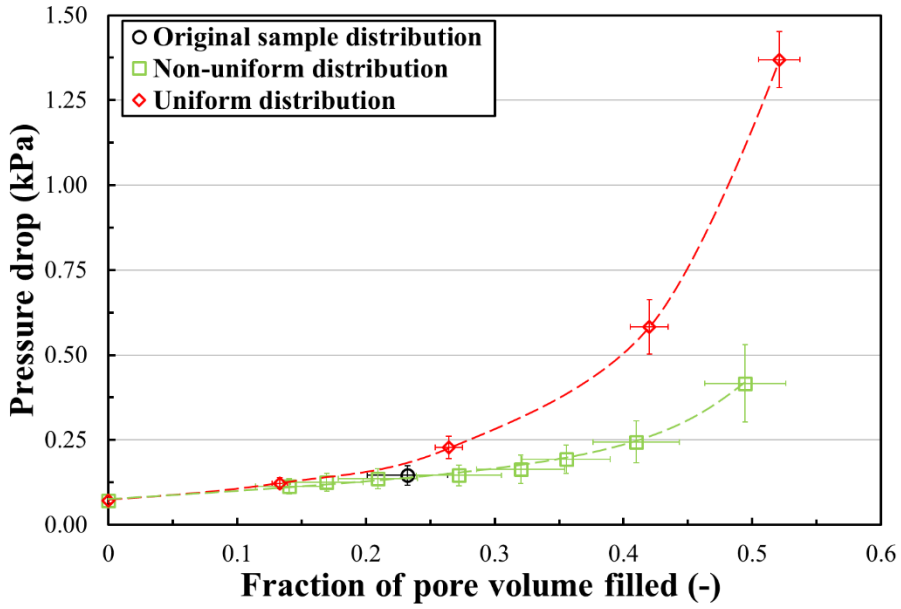

Figure 11: Comparison of the pressure drops (ΔP) predicted by the LBM-based numerical model as a function of the amount of washcoat (f_w) for the two washcoat distribution profiles in the reconstructed GPF porous wall structures. The dashed lines are a guide for the eye, and the error bars represent the standard deviations of the reported mean values for the four wall subdomains.

Results show a near-exponential increase in the pressure drop as the pore volume is filled with catalyst. Significant differences in pressure drop between the two sets of washcoat profiles are only noticeable when f_w > ~20-25%, which corresponds roughly to amounts of washcoat greater than

that used for the OS sample. When $f_w \approx 50\%$, a roughly 3-fold higher pressure drop is predicted with the uniform profile.

3.3 Soot capture by the reconstructed structures

In this section, the accuracy and performance of the commercial software GeoDict®, which was used for this part of the work, is first assessed. Then, the impact of various washcoat distribution profiles on the capture efficiency of the reconstructed porous walls is examined in detail.

3.3.1 Model assessment and computational performance

Obtaining appropriate capture efficiency data for the GPF porous wall alone is not an easy task as: (1) the overall capture efficiency of a GPF is a sum of several contributions from different origins (e.g. entrance effects, capture into channels through diffusion, porous wall microstructure,…) which are difficult to isolate independently of each other and are intrinsically multiscale, and (2) experimental work reported in the literature often lacks details regarding the exact geometry of these different parts of the GPF and/or the exact operating conditions (e.g. precise soot size and shape distributions), making it difficult to carry out detailed model validation at the wall scale. The validity of the predictions of the FilterDict® module was therefore here assessed using the detailed fibrous filter data published by Lee and Liu (Lee and Liu 1981) and the analytical correlations for fibrous filters provided in Gervais et al. (Gervais et al. 2015).

In the experiments of Lee and Lie (1981), moderately monodisperse aerosols were generated by dissolving a low vapour pressure substance such as DOP (di-octyl phthalate) in a volatile solvent such as alcohol. The mixture was heated and then cooled to obtain monodisperse spherical particles whose diameter could be controlled by adjusting the DOP concentration. An electrical particle detector was used to measure the aerosol concentration upstream and downstream from the filter and to thus retrieve E_f. Two types of fibrous filters were produced for these experiments: filter A, which was made of uniform 11.0 ± 1.06-µm diameter Dacron fibers, and filter B, which was made of uniform 12.9 ± 1.06-µm diameter Dacron fibers. Data from filters A and B, which had porosities within the range of porosities used for the GPF study, are here reported with three air velocities, i.e., 0.01, 0.03, and 0.1 m/s. Since the original filter structures were not readily available but there was sufficient data to recreate them with a good degree of fidelity, corresponding 3D random fiber network structures were created using the FiberGeo® module of GeoDict®. The in-plane

dimensions of the computational domain were 500 µm × 500 µm, and the filter thickness was adjusted to fit the reported values (i.e., 183 µm and 243 µm, respectively, for filters A and B). In addition, 200-µm and 100-µm buffers, respectively, were added upstream and downstream from the filter. The voxel resolution was set at 0.5 µm.

Figure 12 compares the numerical capture efficiency predictions as a function of particle diameter with the experimental data from Lee and Liu (1981) and analytical correlation predictions from Gervais et al. (2015). Although no information was provided on the experimental uncertainty, overall the trends predicted are all in relatively good agreement with those observed experimentally and analytically with respect to the effect of air velocity and soot particle diameter. Nonetheless, numerical simulations tend to overestimate, by a constant bias, the capture efficiency obtained from experimental data and analytical correlations. A detailed analysis is carried out in Appendix D to determine this bias and a corresponding correction is proposed, although it is not applied in the remaining of this paper.

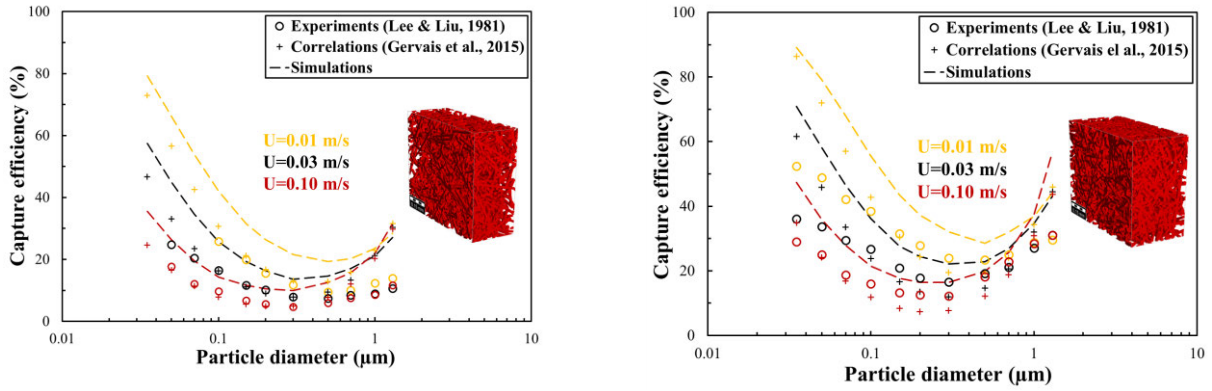

(a) (b)

Figure 12: Comparison between our numerical predictions and experimental data from Lee and Liu for the capture efficiency of (a) fibrous filter A (ε=70.1%, L=183 µm) and (b) fibrous filter B (ε=58.0%, L=243 µm). The insert in each graph represents the reconstructed fibrous structures used for the simulations.

Despite the reported discrepancy in capture efficiency, the overall trends appear to be well predicted, which is satisfactory in the context of a study that focuses on the relative differences between clean porous wall microstructures. In fact, the actual magnitude of the capture efficiency can be affected by many factors. In the case of soot particles in a cordierite-based particulate filter,

the capture efficiency is actually expected to be underestimated by the current methodology for two main reasons: (1) as soots are non-spherical clusters of primary particles, assuming spherical particles will tend to underestimate capture, and (2) as shown recently by (Kočí 2019), substantial soot capture by inertial impaction may take place at the wall surface due to the sudden 90° change in flow direction going from the channel into the wall. Assuming a flow perpendicular to the wall surface can indeed misrepresent the inlet flow condition and thus potentially reduce the capture efficiency, although most of the soot sizes in a GPF are generally less than 200 nm and therefore the number of inertial particles may in fact be limited. A measurement campaign is currently being carried out to validate the model in the PF context.

Lastly, in terms of computational requirements, the computational time for each simulation done with GeoDict® on the 456×400×389-voxel domains for tracking 250 000 particles (25 000 particles for each of the 10 particle diameters investigated) was approximately 6 hours on 2 cores (2.5 GHz Intel Xeon E5-2430V2 processor).

3.3.2 Soot capture efficiency predictions

The soot capture efficiency of the 56 generated structures for various soot sizes was computed using the FilterDict® module of the commercial software GeoDict®. Noticeable differences in the impact of increasing coating amount between the two washcoat uniformity profiles on the capture efficiency can be seen in Figure 13.

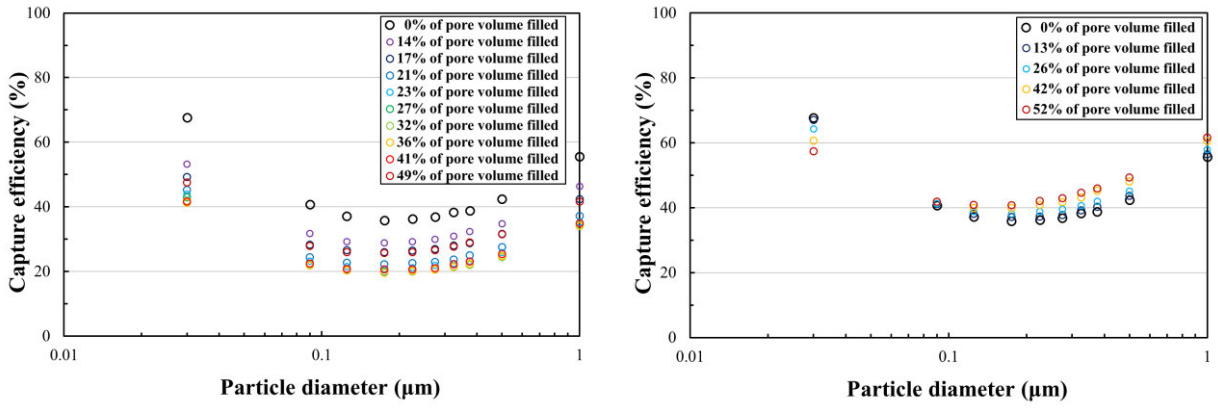

(a) (b)

Figure 13: Soot capture efficiency (E_f) as a function of soot particle diameter (d_p) for a (a) non-uniform and (b) uniform washcoat distribution profiles in Subdomain 4 of the reconstructed GPF porous wall structures.

In the case of a non-uniform profile, capture efficiency is degraded more or less evenly throughout the range of particle diameters while increasing coating amount in the range $0\% \leq f_w \leq 41\%$. This decrease in capture is somewhat surprising and will be explained in more detail later in this section. Beyond this amount of washcoat, the capture starts to increase sharply (as evidenced by the data points at $f_w = 49\%$). For the uniform deposition, the capture efficiency of the very small particles is degraded by an increasing coating amount, whereas a reverse trend is observed for larger particles. The results of Figure 13 show also a minimum capture efficiency at a particle mobility diameter of approximately 200 nm, which is a common value in the PF context (Joshi and Johnson 2018).

For the remainder of the paper, unless stated otherwise, the results are reported in terms of the minimum capture efficiency (i.e., at the most penetrating particle size or MPPS), hereafter referred to as E_f for conciseness. Figure 14 presents the variation of E_f averaged over the four subdomains (Figure 3) for the two sets of profiles, as a function of the pore volume filled.

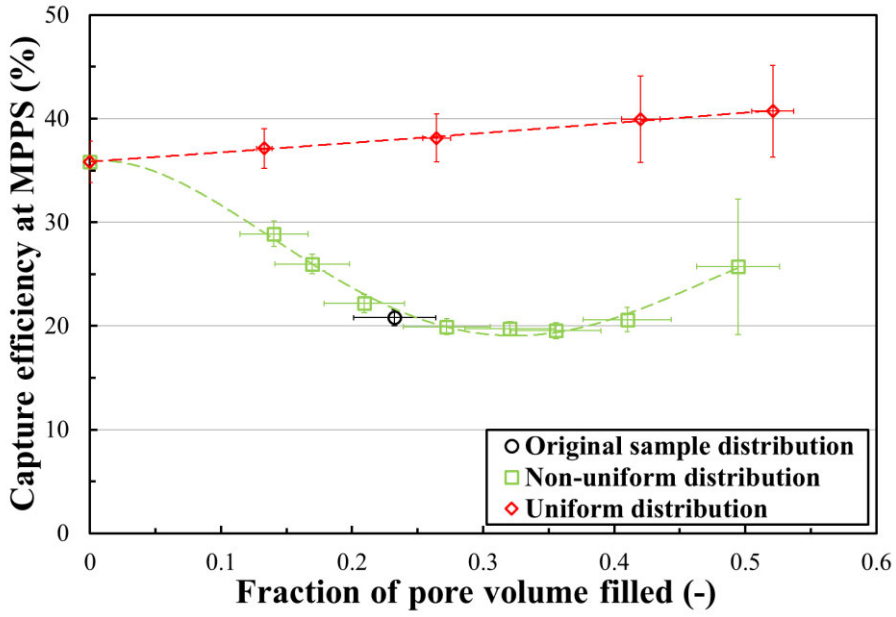

Figure 14: Comparison of soot capture (E_f) at MPPS as a function of the amount of washcoat (f_w) for the two washcoat distribution profiles in the reconstructed GPF porous wall structures. The dashed lines are a guide for the eye, and the error bars represent the standard deviations of the reported mean values for the four wall subdomains (Figure 3).

The range of efficiency values is comparable to those in the literature for clean coated GPFs (Joshi and Johnson 2018). Nonetheless, similarly to what has been reported in Figure 13, two different soot capture efficiency behaviours can be observed at MPPS as the pore space is filled with increasing amounts of washcoat depending on the uniformity of the washcoat distribution profile. In the case of a uniform distribution, as expected, E_f increased gradually as more and more catalyst is added to the pore space. This behaviour can be explained by the gradual decrease in all pore diameters as shown by the mean pore diameter and pore size distribution variations in Figure 6 and Figure 7(b). As each channel being smaller, the soot particles transported by the air flow through the filter wall are more easily captured by interception. At the same time, as evidenced by the decrease in capture at small particle sizes in Figure 13(b), the capture by diffusion slightly decreases as a result of the increase of interstitial velocity (as the superficial velocity is kept constant). Now, for a non-uniform coating profile, similarly to what has been reported in Figure 13(a) and again somewhat surprisingly, the soot capture efficiency at MPPS decreases when f_w is increased from 0% to ~30%, and then begins increasing beyond this point. At first glance, this

result appears to be counter-intuitive as higher soot capture is normally expected when filter porosity decreases (see (Lee and Gieseke 1979; Lee and Liu 1981)), although some contradictory results have also been reported by others (Liu et al. 2018). To date, no comprehensive explanation for this phenomenon can be found in the literature, but this will be clarified in the following.

The great advantage of numerical simulations is that they can be used to correlate filtration performance with the flow and structural characteristics of the porous medium in a way that is much more detailed than what can be achieved experimentally. To determine the detailed mechanisms involved in the decrease in filtration performance with an increase in the amount of washcoat, visualizations of the flow field through the same porous wall section but with two different amounts of washcoat (low and high coating amounts) for the uniform and non-uniform distribution profiles are presented in Figure 15, including a region of particular interest circled in yellow dashes. The flow pathways through this region are very similar, ranging from a low coating amount to a high coating amount when a uniform distribution of washcoat is used. Only the magnitude of the velocity increases as the pores are filled with more washcoat because every pore channel section decreases with an increasing amount of catalyst. In the case of the non-uniform distribution profile, the velocity magnitude is also affected by an increasing amount of washcoat, so are the flow paths, as shown by the disappearance of many small flow channels in the area of interest. This is caused by the complete obstruction of a large number of smaller channels as the amount of catalyst increases, redirecting the flow to larger channels that are not completely clogged and reinforcing the flow channelling effect inherent to such complex porous structures. This observation can provide a good explanation for the decrease in soot capture in the range $0\% \leq f_w \leq \sim 30\%$ for the non-uniform profiles in Figure 14. Indeed, as the amount of washcoat increases in the range $0\% \leq f_w \leq \sim 30\%$, the flow is redirected to larger pore channels in which interstitial velocities are increasing (as the superficial velocity is kept constant and ε is decreasing). As a result, the transported soot particles have less chance to collide with the solid surface of the porous medium both by interception and diffusion, leading to a decrease in E_f. This is also evidenced in Figure 13(a) by the decrease in both diffusion- (below the MPPS) and interception-driven (above the MPPS) capture efficiency values. Beyond these coating amounts, as all small channels are finally clogged, the size of the remaining larger channels gradually decreases, leading to a sharp increase in capture efficiency through the interception mechanism.

Furthermore, a close examination of the pore size distributions in Figure 7 confirms the explanation provided by the visual inspection of the flow fields. As mentioned in Section 3.1, the pore size distributions showed that when $0\% \leq f_w \leq 30\%$, the small pores (i.e., with diameters lower than 20 μm) of the non-uniform profiles are preferentially affected leading to a redirection of the flow to larger, but less capture-efficient channels, whereas all pore sizes are reduced to a similar degree by the addition of washcoat in the case of uniform profiles and thus leading to a gradual increase in soot capture in this case. In addition, when $f_w > 30\%$, larger pores also begin to be affected, which can be seen by the corresponding decrease in the mean pore diameter shown in Figure 6. This corresponds precisely to the onset of the gradual increase in soot capture observed beyond this point in Figure 14. These findings clearly show that there is a very close relationship between filtration performance and the structural characteristics of the porous medium and the impact of the non-uniform washcoat distribution investigated in the present study. However, caution should be exercised in over-generalizing the results in Figure 14, as they have been obtained in specific conditions, i.e. in a clean filter for a given type of non-uniform washcoat distributions under constant flow rate conditions. In fact, in light of these results, the contradictory results reported in the literature regarding the trend in capture efficiency for a non-uniform profile may be explained by different factors: 1) the structural characteristics of the base substrate, 2) the coating non-uniformity and 3) the conditions under which the experiments were carried out (e.g. constant flow velocity or constant pressure drop, presence of soot clogging,…). Here, the numerical experiments were conducted at constant flow rate, which leads to a decrease in capture by diffusion as the interstitial velocity increases for an increasing amount of washcoat. At the same time, experiments conducted at constant pressure drop are expected to result in greater capture by diffusion while they may not show an overall decrease in capture efficiency.

On the basis of capture efficiency results discussed above, it follows that the uniform profiles deposited on the cordierite are up to twice as efficient as the non-uniform profiles, particularly when $f_w \leq 30\%$. However, to be able to judge the intrinsic performance of a filter medium, it is common in the field of air filtration to relate capture efficiency to the pressure drop using the quality factor. This is what we will analyze next.

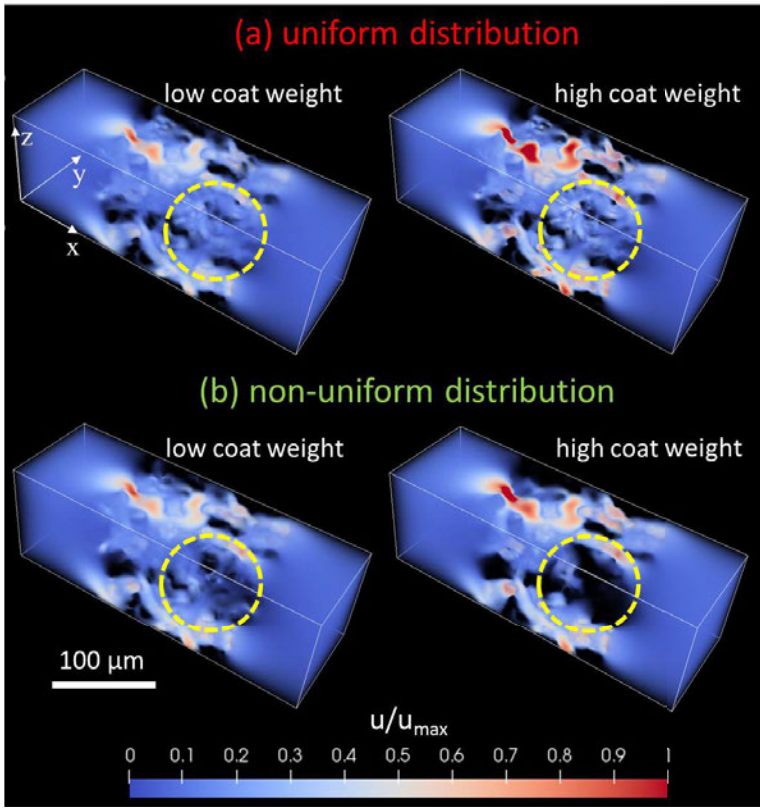

Figure 15: Close-up visualizations of the normalized flow field for the same 456×100×100-voxel porous wall section with two different coating amounts (low and high) and for the two washcoat distribution profiles (uniform and non-uniform). Low and high coating amounts correspond to f_w = 14.0% and 27.2% and f_w = 13.3% and 26.4% for the non-uniform and uniform distribution profiles, respectively. The dashed yellow circles represent regions of interest, in which a significant change in flow pathways takes place as the washcoat profile is changed.

3.4 Overall filtration performance of the reconstructed structures

As previously seen, on the one hand, structures with a non-uniform washcoat distribution presented a lower pressure drop than structures with a uniform washcoat distribution at every washcoat amount studied. On the other hand, soot capture was greater for all structures with a uniform washcoat distribution at a given coating amount. Comparing the two distribution profiles in terms of filtration performance is thus not straightforward if one does not resort to the quality factor as

defined in Eq. (16). Figure 16 presents variations of Q_f as a function of coating amount for the two washcoat distribution profiles.

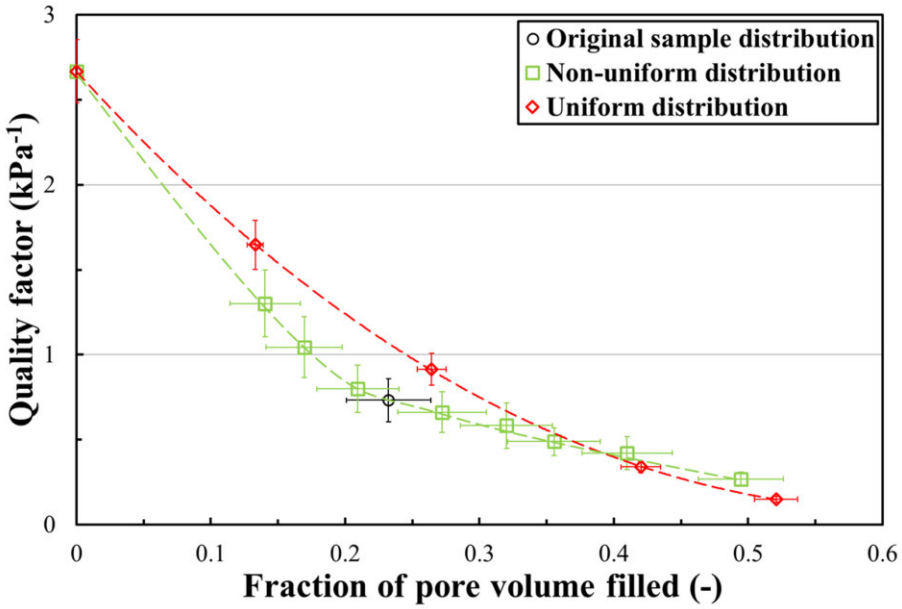

Figure 16: Comparison of quality factors (Q_f) as a function of the amount of washcoat (f_w) for the two washcoat distribution profiles in the reconstructed GPF porous wall structures. A higher Q_f corresponds to a better filtration performance. The dashed lines are a guide for the eye, and the error bars represent the standard deviations of the reported mean values for the four wall subdomains (Figure 3).

The first striking result is that the filtration performance of the porous wall decreases for both washcoat profiles investigated as the coating amount is increased, meaning that the addition of a catalyst for reducing noxious gases is detrimental to the filtration performance of the cordierite substrate. This decrease is quadratic for the uniform deposition profiles throughout the coating amount range investigated. On the other hand, the decrease for the non-uniform deposition profiles is also quadratic, albeit only when $f_w \leq$ ~20% (i.e., up to approximately the OS washcoat profile) and is initially significantly steeper than the trend for the uniform deposition profiles but becomes linear thereafter. Overall, the uniform washcoat deposition profile gives a better filtration performance than the non-uniform deposition profile when $f_w \leq$ ~40%. Beyond this level, no significant advantage to using a uniform deposition is observed and, in fact, the non-uniform deposition profile tested performed slightly better. The greatest relative difference between the two

deposition profiles peaks at 50% when $f_w \approx 20\%$. In addition, a 30% improvement in Q_f could be expected if the OS structure had been manufactured with a uniform washcoat deposition profile. In this regard, these predictions demonstrate how this type of modelling may help GPF manufacturers determine an optimum trade-off between coating amount, filtration performance and catalytic conversion, and help design filters with the best washcoat distribution profile.

4. CONCLUSION

To shed light on the impact of the amount of catalyst and deposition uniformity of the porous wall on the filtration performance of clean catalyst-coated GPFs, a three-step numerical model was developed to (1) reconstruct representative volumes of a GPF porous wall based on X-ray computed tomography data and to create artificial uniform and non-uniform catalyst depositions in its pore space using novel erosion-dilation procedures, (2) compute the permeability and pressure drop of the reconstructed structures by solving the flow field using the LBM, and (3) predict the soot capture efficiency of the reconstructed structures by solving the Langevin equation using GeoDict® software. The accuracy of the model predictions and thus the soundness of the numerical methodology was also assessed using data and correlations from the literature. The impacts of the amount of washcoat and the deposition profiles on permeability, pressure drop, soot capture efficiency, and quality factor of the filter medium were investigated in a systematic way and were correlated to the structural characteristics of the reconstructed media (particularly the mean pore diameter and the pore size distribution). To our knowledge, this is the first time that such a detailed investigation has been conducted.

Despite a significantly higher pressure drop, it was found that a uniform washcoat distribution throughout the clean GPF wall resulted in significantly better filtration performance than a non-uniform washcoat distribution in terms of soot capture efficiency (up to 100% improvement) and quality factor (up to 50% improvement) for up to 40 % of pore volume filled with catalyst. Interestingly, as previously reported by some literature data (Liu et al. 2018; Joshi and Johnson 2018), our numerical results showed that increasing the amount of washcoat can counter-intuitively result in a decrease in soot capture if it is non-uniformly deposited in the pore space as this leads to a strengthening of flow channeling. This was revealed by detailed visualizations of the flow field and analysis of the pore size distribution. However, caution should be exercised when extrapolating the findings reported here to all non-uniform washcoat deposition profiles and to all ceramic

substrates. These findings call for a more thorough investigation of various forms of non-uniform and ceramic substrates with a focus on structures, for which a process or device exists to produce them.

Lastly, the present study is a first step toward building a more comprehensive model that not only predicts GPF wall filtration performance but also the chemical conversion of noxious gases by the catalyst, and that will ultimately provide more information on the effectiveness of washcoats. A more comprehensive model that makes use of an LBM scheme for solving an advection-diffusion-reaction equation for the GPF porous wall will be presented in an upcoming paper (Belot et al. To be submitted (2020)). Once fully developed, the model will become a valuable design tool that will provide guidance to catalyst-coated GPF manufacturers as well as insights into why specific catalyst coatings perform better than others.

ACKNOWLEDGMENTS

This research was supported by the Natural Sciences and Engineering Research Council of Canada through a Strategic Partnership Grant (STPGP-493797-16) and a Grant from the Collaborative Research and Training Experience (CREATE-481695-2016) program in Simulation-based Engineering Science (Génie Par la Simulation). The authors would also like to thank Calcul Québec/Compute Canada for the computational resources and support provided.

APPENDIX A – DEFINITION OF A REPRESENTATIVE ELEMENTARY VOLUME FOR THE RECONSTRUCTED STRUCTURES

To ensure that the domain size is large enough so as to not influence the permeability predictions and that it can thus be considered as a Representative Elementary Volume (REV) of the pore space, the Brinkman screening length, defined as the distance over which velocity disturbances caused by an individual flow obstacle decay to the bulk fluid velocity, is commonly used (Clague and Phillips 1997). This length scale is equal to the square root of Darcy's permeability (i.e., $\sqrt{k_D}$). To determine a permeability measurement independent of the domain size, the Brinkman screening length criterion prescribes that $\ell \gg \sqrt{k_D}$, where ℓ is the domain characteristic dimension. For all the structures investigated, knowing that $0.4\ \mu m^2 \leq k_D \leq 8\ \mu m^2$, $\ell \gg \sim 3\ \mu m$ would thus be required according to this criterion. Partitioning the OS sample wall structure into four subdomains (as in Figure 3) and up to 16 subdomains would thus easily fulfill this requirement as 16 subdomains would result in $\ell \cong 200\ dx \approx 250\ \mu m$. To further verify that the number of subdomains does not influence permeability, a comparison between the mean permeability computed on 4, 9, and 16 subdomains with the mean permeability computed over the entire wall structure has been carried out and is presented in Figure 17. The results show a slight increase in the discrepancies with respect to the number of subdomains, i.e., 2.6%, 7.5%, and 11.0% for 4, 9 and 16 subdomains, respectively, as well as an increase in the variability from subdomain to subdomain, as shown by the standard deviations plotted as error bars. The increase in discrepancies can be attributed to the symmetric boundary conditions added at the lateral boundaries of the subdomains created. The increase in variability from subdomain to subdomain can be attributed to the large-scale heterogeneity of the cordierite structure, which is well above the Brinkman screening length. As such, this result clearly underlines the fact that the Brinkman screening length criterion is a necessary condition but not a sufficient one for guaranteeing the domain size independence of the flow computation for such heterogenous porous media. Another important criterion that should be taken into consideration is the mean pore size, which in this study ranges from 10 to 30 μm (see Figure 6). Also, every partition considered for this REV study resulted in subdomains that were at least one order of magnitude larger than the mean pore size. Nevertheless,

the partition of the OS sample domain into four subdomains seems to be a good trade-off between ease of computation and accuracy, which is why it was chosen in the present study.

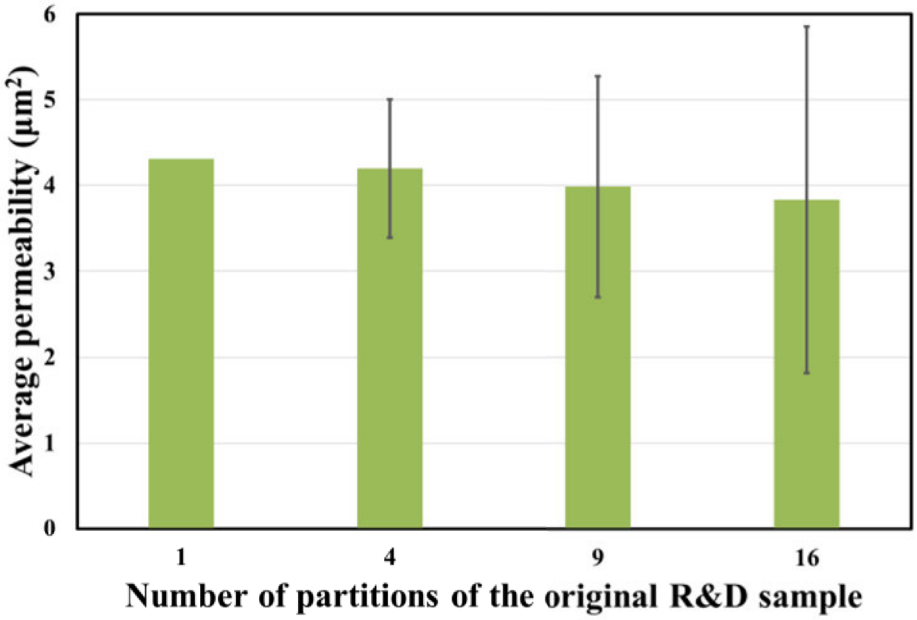

Figure 17: Comparison of the average permeabilities obtained for different partitioning schemes of the whole OS sample. The error bars represent the standard deviations of the permeability values computed on all the partitions for a given partitioning scheme.

APPENDIX B - CORRELATION FUNCTIONS OF THE RECONSTRUCTED STRUCTURES

Additional statistical structural descriptors, namely the two-point probability function and the lineal path, are provided here. They may help reconstruct the artificial structures created in this work using the simulated annealing technique (Matte-Deschênes et al. 2016), for instance, to enable future use of these structures by any interested reader. Both correlation functions were computed on the solid phase (i.e., cordierite + catalyst) of each structure reconstructed from Subdomain 1 of the OS sample.

The probability that n points at positions $(x_1, x_2, \ldots, x_n)$ in the medium are in phase i is denoted by ${S_n}^i$. Here, we only considered two phases, i.e., the solid phase (cordierite + catalyst, with $i = 1$) and the void phase (with $i = 0$). Based on this definition, for an isotropic medium, the two-point probability function is given by:

$$S_2{}^i(r) = \frac{n_i(r)}{n_t(r)} \tag{17}$$

where $n_i(r)$ and $n_t(r)$ are, respectively, the number of pairs of phase *i* voxels and the total number of pairs of voxels of any phase separated by distance *r*. Interestingly, both global descriptors ε and S_0 can be obtained from the two-point probability function for any 3D digitized porous medium as $\varepsilon = S_2{}^0(0)$ and $S_0 = -6\frac{dS_2{}^0}{dr}(0)$ (Yeong and Torquato 1998b, 1998a). In addition to the two-point probability functions, another spatial correlation function that is very useful for characterizing porous media is the lineal-path function given by (Torquato 2002):

$$L^i(r) = \frac{m_i(r)}{m_t(r)} \tag{18}$$

where $m_i(r)$ and $m_t(r)$ are the number of segments of length *r* wholly fitting in phase *i* when randomly thrown into the sample and the total number of fitting attempts, respectively. This correlation function provides interesting information on the connectiveness of phase *i* in the structure and can serve for reconstruction algorithms (Havelka, Kucerova, and Sykora 2016; Torquato 2002). In the present study, the $S_2{}^i(r)$ and $L^i(r)$ functions were calculated using a custom-written program based on a procedure described in the literature (Torquato 2002).

The two-point probability and lineal-path functions calculated in a direction perpendicular to the flow in the GPF porous wall structures reconstructed from Subdomain 1 for the uniform and non-uniform deposition profiles with various amounts of washcoat are presented in Figure 18 and Figure 19.

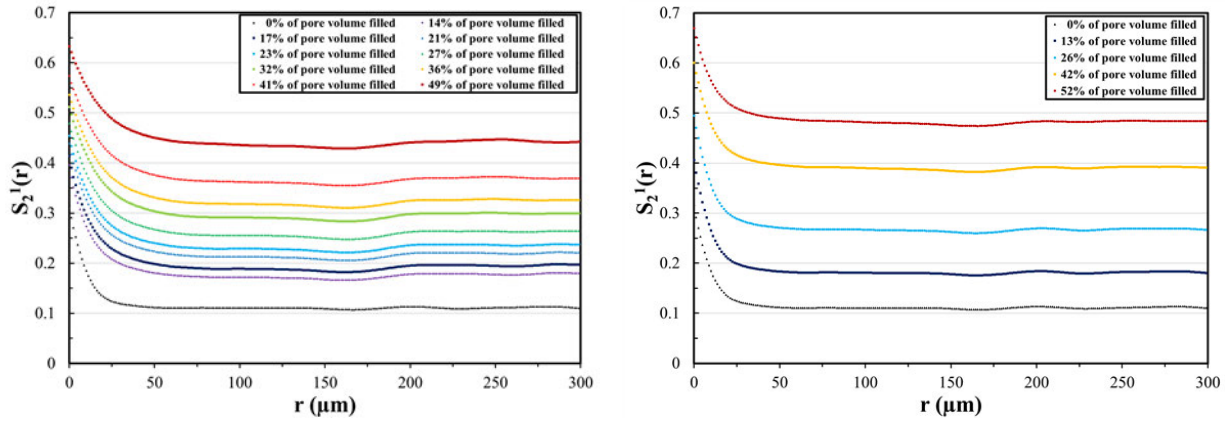

(a) (b)

Figure 18: Two-point probability functions calculated for a (a) non-uniform and (b) uniform washcoat distribution profiles of the GPF porous wall structures reconstructed from Subdomain 1 of the OS sample.

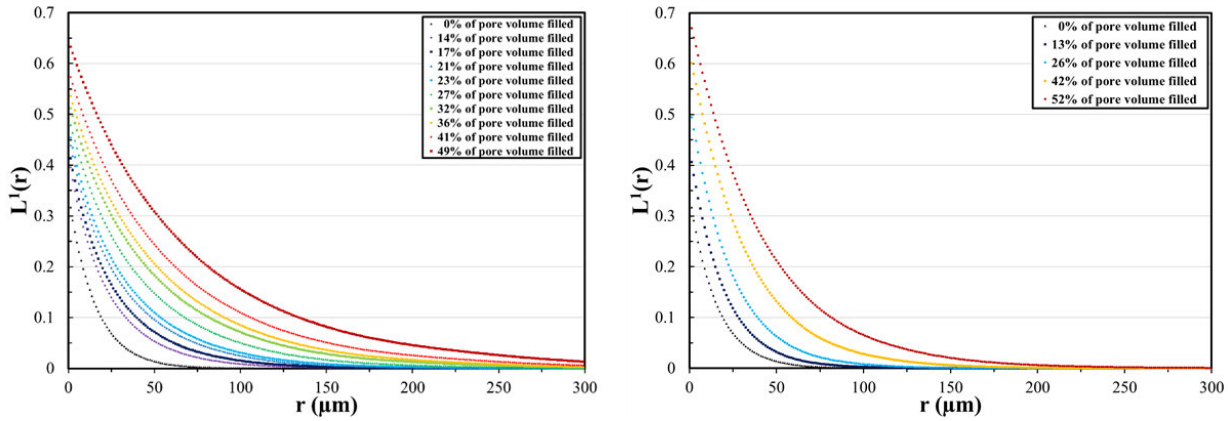

(a) (b)

Figure 19: Lineal-path functions calculated for a (a) non-uniform and (b) uniform washcoat distribution profiles of the GPF porous wall structures reconstructed from Subdomain 1 of the original OS sample.

APPENDIX C - COMPARISON OF THE OBTAINED PERMEABILITY TRENDS WITH LITERATURE DATA

Although the SiC-based ceramic substrate used by Konstandopoulos et al. (Konstandopoulos, Kostoglou, and Vlachos 2006) was structurally different, and although the characteristics of the non-uniform washcoat depositions were not reported, a qualitative comparison with their results was attempted in Figure 20, which presents the trends obtained in terms of normalized permeability as a function of the amounts of washcoat for the uniform and non-uniform distribution profiles reported together with those presented in Figure 10. The SiC-based structures with uniform distributions of washcoat displayed similar quadratic decreases in permeability as a function of the amount of washcoat deposited on the bare ceramic. Note that while the trends are similar, they are not identical as the bare substrate can obviously play a determining role. In addition, while both studies reported a smaller decrease in permeability as a function of the amount of washcoat for the non-uniform washcoat profiles than for the uniform ones, the difference between the uniform and non-uniform distribution profiles reported by Konstandopoulos et al. is much more pronounced than the one obtained in the present study. In comparison, the decrease in permeability for the non-uniform profiles with respect to the permeability of the bare substrate was actually more limited (~ 20 % at $f_w = 30$ %) whereas it is approximately 50% in our numerical experiments for the same amount of washcoat. This difference can be attributed to the nature of the non-uniformity created, which unfortunately was not reported by the authors. Indeed, while there is only one uniform profile at a given coating amount on a given ceramic substrate, there is a quasi-infinite number of possible non-uniform profiles. Some might be better than others, although not all of them are necessarily achievable in practice. It should be remembered that, in the present study, the non-uniformity of the OS sample was decreased or amplified using an erosion-dilation algorithm. This created non-uniform profiles that were more permeable that their uniform counterparts. However, other types of non-uniformity could possibly have more or less impact. As already suggested, in addition to the nature of the non-uniformity, the magnitude of the impact may be also strongly influenced by the ceramic structure used as a substrate.

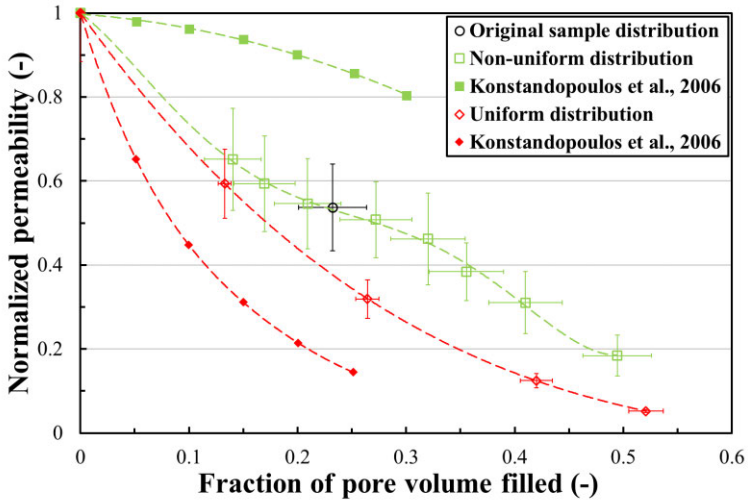

Figure 20: Comparison of permeabilities (normalized to the permeability of the bare wall) as a function of the amount of washcoat for the two washcoat distribution profiles as predicted by the proposed model and by (Konstandopoulos, Kostoglou, and Vlachos 2006). The dashed lines are a guide for the eye, and the error bars represent the standard deviations of the reported mean values for the four wall sections.

APPENDIX D –DISCREPANCY IN FILTRATION EFFICIENCY PREDICTIONS BETWEEN EXPERIMENTS AND SIMULATIONS

As noted in Section 3.3.1, there appears to be a constant bias between experimental and numerical predictions of capture efficiency for the partial experimental data set presented (i.e., for filters having porosities in the range of porosities used in the GPF study). In this appendix, an attempt is made to determine this bias for the entire data set from Lee and Liu (1981). It is possible to show that the following simple expression can be used to correct the capture efficiency predictions for a constant bias:

$$E_{f,corr} = 1 - P_{p,sim}^{\alpha} = 1 - \left(1 - E_{f,sim}\right)^{\alpha} \tag{19}$$

where $E_{f,corr}$ and $E_{f,sim}$ are, respectively, the corrected and originally computed capture efficiencies, $P_{p,sim}$ is the corresponding particle penetration and α is the correction factor. A minimization of the mean square difference between numerical and experimental data for the 11 filter configurations and operating conditions reported in Lee and Liu (1981) is carried out by varying systematically the correction factor through a list of possible fractions defined as $\alpha \in \left\{\frac{1}{2}, \frac{4}{7}, \frac{8}{13}, \frac{2}{3}, \frac{8}{11}, \frac{4}{5}, 1\right\}$. Figure 21 shows that a correction factor of $\frac{2}{3}$ leads to the best agreement between simulations and experiments bringing the mean relative difference for the entire data set from 40.7 % down to 17.0 %. Figure 22 shows the excellent improvement in the agreement between numerical, experimental and analytical predictions once the $\frac{2}{3}$ correction factor is applied.

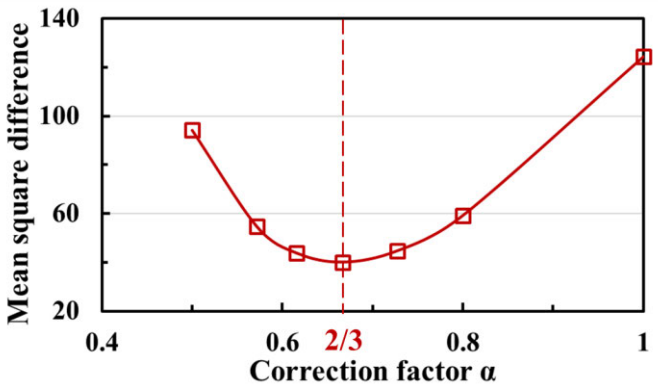

Figure 21: Mean square difference between numerical calculations using GeoDict® and experimental data from Lee and Liu (1981) and calculated on the 11 filter configurations.

Although further simulations and experiments would be required to identify the exact cause of this correction factor, it is interesting to point out that Yeong and Torquato (Yeong and Torquato 1998b, 1998a) reported an inherent overestimation of S_o for a voxelized porous structure, such as the ones used in this study, by a constant factor of $\frac{3}{2}$ because of the staircase-like fractal nature of such surface representation. As the single collector efficiency (i.e. $\beta\eta$ in Eq. (10)) is proportional to S_o (through d_c), an overestimation of $\frac{3}{2}$ of the single collector efficiency could be expected and a

correction of analytical predictions by a $\frac{2}{3}$ factor would thus be required. However, it is not yet clear how the fractal nature of the pore space would influence the numerical solution of the Langevin problem such that a constant bias would result, and this could be the result of a mere coincidence.

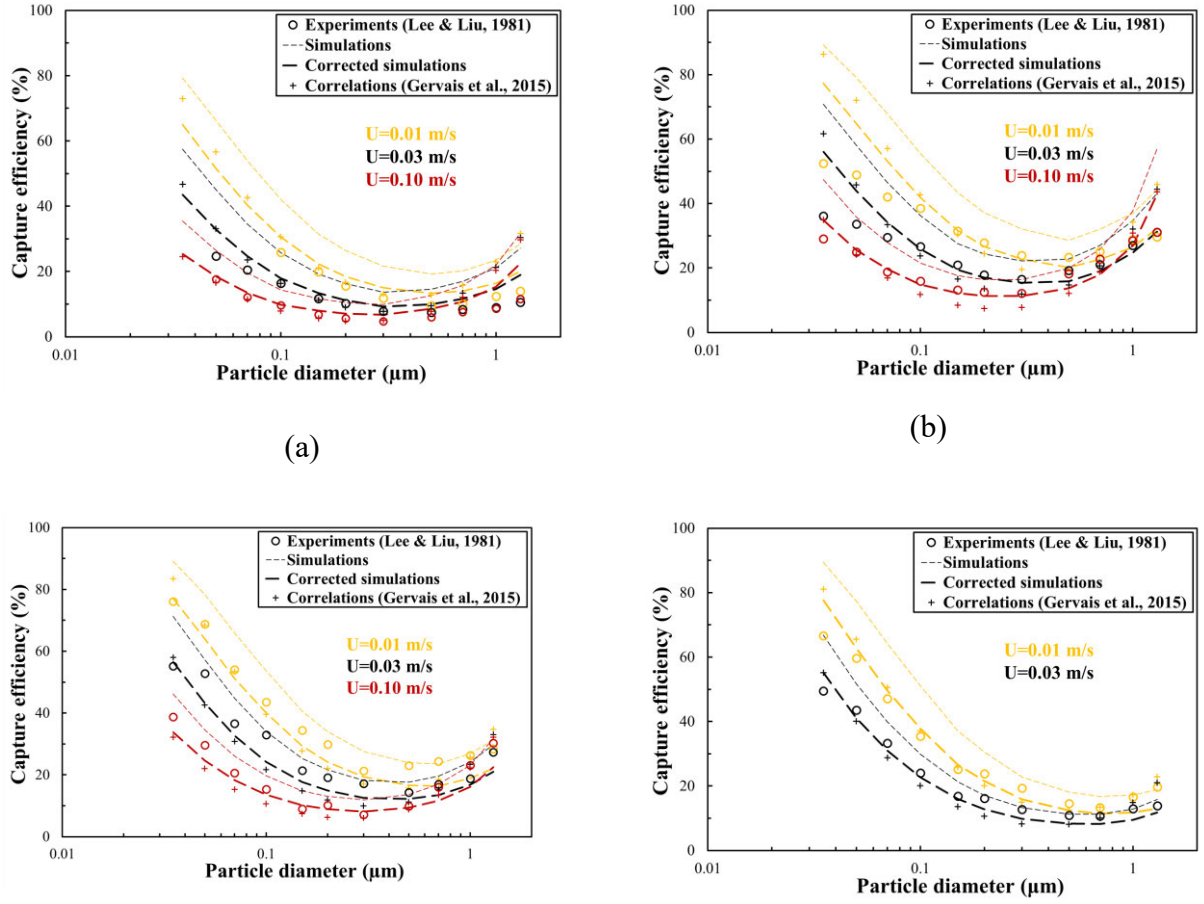

Figure 22: Comparison between the numerical predictions using $\alpha = 1$ (uncorrected) and $\alpha = \frac{2}{3}$ (corrected), experimental data from Lee and Liu (1981) and correlations from Gervais et al. (2015) for the capture efficiency at various superficial velocities of (a) fibrous filter A with ε=70.1% and L=183 µm, (b) fibrous filter B with ε=58.0% and L=243 µm, (c) fibrous filter B with ε=72.9% and L=368 µm, and (d) fibrous filter B with ε=90.4% and L=1029 µm.

REFERENCES

Aderhold, Dirk, Alan Haynes, Georges, Michael Spencer, Leonard, William, and Duncan Winterbourn, John, William. 1999. "Monolith Coating Apparatus and Method Therefor." In *International Search Report.*: Wishart, Ian, Carmichael.

Azimian, Mehdi, Liping Cheng, and Andreas Wiegmann. 2017. "Simulation of soot filtration in diesel particulate filter with GeoDict." In *15th FAD-Conference "Challenge- Exhaust Aftertreatment for Diesel Engines"*. Dresden, Germany.

Becker, Jürgen, Liping Cheng, Cornelia Kronsbein, and Andreas Wiegmann. 2016. 'Simulation of Cake Filtration for Polydisperse Particles', *Chemical Engineering & Technology*, 39: 559-66.

Belot, Igor, Yixun Sun, David Vidal, Martin Votsmeier, Philippe Causse, Robert Hayes, François Trochu, and François Bertrand. To be published (2020). '3D Additive Manufacturing for Validation of a Microscale Numerical Model for Permeability Prediction of Coated Particulate Filters ', *Chemical Engineering Journal*.

Belot, Igor, David Vidal, Robert Greiner, Martin Votsmeier, Robert Hayes, and François Bertrand. To be submitted (2020). 'Numerical Investigation of the Impact of Washcoat Distribution on the Catalyst Performance of Gasoline Particulate Filters', *Chemical Engineering Science*.

Bensaid, S., D. L. Marchisio, D. Fino, G. Saracco, and V. Specchia. 2009. 'Modelling of diesel particulate filtration in wall-flow traps', *Chemical Engineering Journal*, 154: 211-18.

Bertrand, François, Christophe Devals, David Vidal, Cyrille Séguineau de Préval, and Robert E. Hayes. 2012. 'Towards the simulation of the catalytic monolith converter using discrete channel-scale models', *Catalysis Today*, 188: 80-86.

Bhatnagar, PL, EP Gross, and M Krook. 1954. 'A model for collision processes in gases. I. Small amplitude processes in charged and neutral one-component systems', *Phys Rev*, 94:511–25.

Bird, R. Byron, Warren E. Stewart, and Edwin N. Lightfoot. 2007. *Transport Phenomena* (John Wiley & Sons, Inc.).

Bissett, E. J., and Farhang Shadman. 1985. 'Thermal Regeneration of Diesel-Particulate Monolithic Filters', *AICHE Journal*, 31: 753-58.

Blake, F. C. 1922. *Trans. Amer. Inst. Chem. Engrs.*, 14: 415-21.

Braisher, Mike, Richard Stone, and Phil Price. 2010. 'Particle Number Emissions from a Range of European Vehicles', *SAE International*.

Clague, David S., and Ronald J. Phillips. 1997. 'A numerical calculation of the hydraulic permeability of three-dimensional disordered fibrous media', *Phys. Fluids*, 9.

Crowe, Clayton T. 2005. *Multiphase Flow Handbook* (Taylor & Francis Group: Boca Raton).

Davis, S.C., S.E. Williams, R.G. Boundy, and S Moore. 2016. "Vehicle Technologies Market Report." In.: Oak Ridge National Lab, ORNL.

Dullien, F. A. L. 1979. *Porous media – fluid transport and pore structure* (Academic Press: New York, NY, USA).

"European Vehicle Market Statistics." In. 2017. *Pocketbook 2017/18*. Berlin: International Council on Clean Transportation.

Foerster, Martin, Ewald Dittrich, Gerhard Birtigh, Walter Leibold, Bernd Mergner, Michael Hoffmann, Wolfgang Hasselmann, and Robert Schafer. 2000. "Process for the coating of the flow channels of a honeycomb form catalytic converter carrier with a dispersion coating." In.: Degussa-Huls Aktiengesellschaft.

"GeoDict." In. 2018. www.geodict.com: Math2Market GmbH.

Gervais, P. C., S. Bourrous, F. Dany, L. Bouilloux, and L. Ricciardi. 2015. 'Simulations of filter media performances from microtomography-based computational domain. Experimental and analytical comparison', *Computers & Fluids*, 116: 118-28.

Gong, Jian, Mark L. Stewart, Alla Zelenyuk, Andrea Strzelec, Sandeep Viswanathan, David A. Rothamer, David E. Foster, and Christopher J. Rutland. 2018. 'Importance of filter's microstructure in dynamic filtration modeling of gasoline particulate filters (GPFs): Inhomogeneous porosity and pore size distribution', *Chemical Engineering Journal*, 338: 15-26.

Graves, Brian Mackenzie, Charles Robert Koch, and Jason Scott Olfert. 2017. 'Morphology and volatility of particulate matter emitted from a gasoline direct injection engine fuelled on gasoline and ethanol blends', *Journal of Aerosol Science*, 105: 166-78.

Greiner, Robert, Torben Prill, Oleg Iliev, Barry A. A. L. van Setten, and Martin Votsmeier. 2019. 'Tomography based simulation of reactive flow at the micro-scale: Particulate filters with wall integrated catalyst', *Chemical Engineering Journal*, 378.

Guan, B., R. Zhan, H. Lin, and Z. Huang. 2015. 'Review of the state-of-the-art of exhaust particulate filter technology in internal combustion engines', *J Environ Manage*, 154: 225-58.

Havelka, Jan, Anna Kucerova, and Jan Sykora. 2016. 'Compression and Reconstruction of Random Microstructures using Accelerated Lineal Path Function', *arXiv:1601.04359 [cond-mat.mtrl-sci]*.

Hayashi, Hidemitsu, and Shuichi Kubo. 2008. 'Computer simulation study on filtration of soot particles in diesel particulate filter', *Computers & Mathematics with Applications*, 55: 1450-60.

Hinds, William C. 1999. *Aerosol Technology : Properties, Behavior, and Measurement of Airborne Particles - 2nd ed.* (John Wiley & sons, Inc.).

Inoda, Satoru, Yasutaka Nomura, Hirotaka Ori, and Yuji Yabuzaki. 2017. "Development of New Coating Technology Optimized for Each Function of Coated GPF." In *SAE Technical Paper Series*.

Joshi, Ameya, and Timothy V. Johnson. 2018. 'Gasoline Particulate Filters—a Review', *Emission Control Science and Technology*, 4: 219-39.

Karamitros, Dimitrios, and Grigorios Koltsakis. 2017. 'Model-based optimization of catalyst zoning on SCR-coated particulate filters', *Chemical Engineering Science*, 173: 514-24.

Keskinen, Jorma, Annele Virtanen, Peter Ahlvik, and Leonidas Ntziachrstos. 1998. 'Estimation of effective Density of Diesel Particles', *J. Aerosol Sci.*, 29: S1007-S08.

Kočí, Petr. 2019. "Multi-scale modeling of catalytic particulate filtes for gasoline engines (GPF)." In *International Symposium on Modeling of Exhaust-Gas After-Treatment (MODEGAT VI)*. Bad Herrenalb/Karlsrue , Germany.

Kočí, Petr, Martin Isoz, Marie Plachá, Adéla Arvajová, Marek Václavík, Miloš Svoboda, Emily Price, Vladimír Novák, and David Thompsett. 2019. '3D reconstruction and pore-scale modeling of coated catalytic filters for automotive exhaust gas aftertreatment', *Catalysis Today*, 320: 165-74.

Koltsakis, Grigorios, Onoufrios Haralampous, Christopher Depcik, and J. Colter Ragone. 2013. 'Catalyzed diesel particulate filter modeling', *Reviews in Chemical Engineering*, 29: 1-61.

Kong, Hyeonoh, and Kazuhiro Yamamoto. 2018. 'Simulation on soot deposition in in-wall and on-wall catalyzed diesel particulate filters', *Catalysis Today*.

Konstandopoulos, A.G., M. Kostoglou, and N. Vlachos. 2006. 'The multiscale nature of diesel particulate filter simulation', *Int. J. Vehicle Design*, 41: 256-84.

Konstandopoulos, Athanasios G. 2000. 'Fundamental Studies of Diesel Particulate Filters: Transient Loading, Regeneration and Aging', *SAE Int. J. Engines*.

Konstandopoulos, Athanasios G., and Eleni Papaioannou. 2008. 'Update on The Science and Technology of Diesel Particulate Filters', *KONA Powder and Particle Journal*, 26.

Kozeny, J. 1927. *Sitzungsber. Akad. Wiss. Wien, Abt. IIa*, 136: 271-306.

Krüger, Timm, Halim Kusumaatmaja, Alexandr Kuzmin, Orest Shardt, Goncalo Silva, and Erlend Magnus Viggen. 2017a. *The Lattice Boltzmann Method: Principles and Practice* (Springer International Publishing).

———. 2017b. *The Lattice Boltzmann: Method Principles and Practice* (Springer International Publishing).

Lambert, Christine, Timothy Chanko, Douglas Dobson, Xin Liu, and James Pakko. 2017. 'Gasoline Particle Filter Development', *Emission Control Science and Technology*, 3: 105-11.

Lambert, Christine K., Mira Bumbaroska, Douglas Dobson, Jon Hangas, James Pakko, and Paul Tennison. 2016. 'Analysis of High Mileage Gasoline Exhaust Particle Filters', *SAE Int. J. Engines*, 01.

Lee, Da Young, Gi Wook Lee, Kyu Yoon, Byoungjin Chun, and Hyun Wook Jung. 2018. 'Lattice Boltzmann simulations for wall-flow dynamics in porous ceramic diesel particulate filters', *Applied Surface Science*, 429: 72-80.

Lee, K. W., and B. Y. H. Liu. 1981. 'Experimental Study of Aerosol Filtration by Fibrous Filters', *Aerosol Science and Technology*, 1: 35-46.

Lee, Kyoo Won, and James A. Gieseke. 1979. 'Collection of Aerosol Particles by Packed Beds', *Environmental Science & Technology*, 13: 466-70.

Lewtas, J. 2007. 'Air pollution combustion emissions: characterization of causative agents and mechanisms associated with cancer, reproductive, and cardiovascular effects', *Mutat Res*, 636: 95-133.

Liu, Xin, Timothy Chanko, Christine Lambert, and Matti Maricq. 2018. "Gasoline Particulate Filter Efficiency and Backpressure at Very Low Mileage." In *SAE Technical Paper Series*.

Lopez-Gonzalez, D., M. N. Tsampas, A. Boréave, L. Retailleau-Mevel, M. Klotz, C. Tardivat, B. Cartoixa, K. Pajot, and P. Vernoux. 2015. 'Mixed Ionic–Electronic Conducting Catalysts for Catalysed Gasoline Particulate Filters', *Topics in Catalysis*, 58: 1242-55.

Lupše, Janez, Marina Campolo, and Alfredo Soldati. 2016. 'Modelling soot deposition and monolith regeneration for optimal design of automotive DPFs', *Chemical Engineering Science*, 151: 36-50.

Matte-Deschênes, Guillaume, David Vidal, François Bertrand, and Robert E. Hayes. 2016. 'Numerical investigation of the impact of thermophoresis on the capture efficiency of diesel particulate filters', *The Canadian Journal of Chemical Engineering*, 94: 291-303.

Mikulic, Dr.-Ing. Ingo, Hein Koelman, Steve Majkowski, and Paul Vosejpka. 2010. "A Study about Particle Filter Application on a State-of-the-Art Homogeneous Turbocharged 2L DI Gasoline Engine." In *Aachener Kolloquium Fahrzeug- und Motorentechnik 2010*.

Ohser, J., and F. Mücklich. 2000. *Statistical Analysis of Microstructures in Materials Science* (Wiley and Sons).

"OpenFOAM." In.

Platt, S. M., I. El Haddad, S. M. Pieber, A. A. Zardini, R. Suarez-Bertoa, M. Clairotte, K. R. Daellenbach, R. J. Huang, J. G. Slowik, S. Hellebust, B. Temime-Roussel, N. Marchand, J. de Gouw, J. L. Jimenez, P. L. Hayes, A. L. Robinson, U. Baltensperger, C. Astorga, and A. S. H. Prevot. 2017. 'Gasoline cars produce more carbonaceous particulate matter than modern filter-equipped diesel cars', *Sci Rep*, 7: 4926.

Rappé, Kenneth G. 2014. 'Integrated Selective Catalytic Reduction–Diesel Particulate Filter Aftertreatment: Insights into Pressure Drop, NOx Conversion, and Passive Soot Oxidation Behavior', *Industrial & Engineering Chemistry Research*, 53: 17547-57.

Richter, Joerg Michael, Raoul Klingmann, Stephanie Spiess, and Ka-Fai Wong. 2012. 'Application of Catalyzed Gasoline Particulate Filters to GDI Vehicules ', *SAE Int. J. Engines*, 5.

Shimrock, Thomas, R. Dirk Taylor, and Jr. John M. Collins. 1985. "Method of Impregnating Ceramic Monolithic Structures with Predetermined Amounts of Catalyst." In.: Engelhard Corporation

Soille, Pierre. 1999. *Morphological Image Analysis, Principles and Applications* (Springer: Berlin).

Stewart, M., TR Gallant, DH Kim, GD Maupin, and A Zelenyuk. 2010. 'Fuel Efficient Diesel Particulate Filter (DPF) Modeling and Development', *Pacific Northwest National Laboratory*.

Stewart, Mark , David Rector, George Muntean, and Gary Maupin. 2004. 'A Mechanistic Model for Particle Deposition in Diesel Particluate Filters using the Lattice-Boltzmann Technique', *Ceramic Engineering and Science Proceedings*.

Swanson, J., W. Watts, D. Kittelson, R. Newman, and R. Ziebarth. 2013. 'Filtration Efficiency and Pressure Drop of Miniature Diesel Particulate Filters', *Aerosol Science and Technology*, 47: 452-61.

Tanaka, Atsushi, Naoto Miyoshi, and Akemi Sato. 2018. "Development of Low Pressure and High Performance GPF Catalyst." In *SAE Technical Paper Series*.

Thomas, C. R., J. A. Pihl, M. J. Lance, T. J. Toops, J. E. Parks, and J. Lauterbach. 2019. 'Effects of four-mode hydrothermal aging on three-way catalysts for passive selective catalytic reduction to control emissions from lean-burn gasoline engine', *Applied Catalysis B: Environmental*, 244: 284-94.

Thomas, Dominique, Augustin Charvet, Nathalie Bardin-Monnier, and Jean-Christophe Appert-Collin. 2017. *Aerosol Filtration* (Elsevier Science).

Torquato, S. 2002. *Random Heterogeneous Materials Microstructure and Macroscopic Properties* (Springer).

Torregrosa, A. J., J. R. Serrano, F. J. Arnau, and P. Piqueras. 2011. 'A fluid dynamic model for unsteady compressible flow in wall-flow diesel particulate filters', *Energy*, 36: 671-84.

Tsuneyoshi, K., O. Takagi, and K. Yamamoto. 2011. 'Effects of Washcoat on Initial PM Filtration Efficiency and Pressure Drop in SiC DPF', *SAE Technical Paper*, 01: 10.

Tsushima, Shohji, Issei Nakamura, Satoshi Sakashita, Shuichiro Hirai, and Daisuke Kitayama. 2010. 'Lattice Boltzmann Simulation on Particle Transport and Captured Behaviors in a 3D-Reconstructed Micro Porous DPF', *SAE International*.

Vadeiko, I., and F. Drolet. 2009. 'A fourth-order algorithm for solving the multi- dimensional Kramers equation in Langevin form', *Journal of Physics A: Mathematical and Theoretical*, 42.

Vidal, David, Igor Belot, Jean-Michel Tucny, and François Bertrand. To be published (2020). 'On the Validation of Capture Efficiency Calculated from Digitized Filter Structures', *J. Aerosol Sci.*

Vidal, David, Cathy Ridgway, Grégoire Pianet, Joachim Schoelkopf, Robert Roy, and François Bertrand. 2009. 'Effect of particle size distribution and packing compression on fluid permeability as predicted by lattice-Boltzmann simulations', *Computers & Chemical Engineering*, 33: 256-66.

Vidal, David, Robert Roy, and François Bertrand. 2010a. 'On improving the performance of large parallel lattice Boltzmann flow simulations in heterogeneous porous media', *Computers & Fluids*, 39: 324-37.

———. 2010b. 'A parallel workload balanced and memory efficient lattice-Boltzmann algorithm with single unit BGK relaxation time for laminar Newtonian flows', *Computers & Fluids*, 39: 1411-23.

Wang, Jihui, Hong Chen, Zhicheng Hu, Mingfa Yao, and Yongdan Li. 2014. 'A Review on the Pd-Based Three-Way Catalyst', *Catalysis Reviews*, 57: 79-144.

Watling, Timothy C., Maya R. Ravenscroft, Jason P. E. Cleeton, Ian D. Rees, and David A. R. Wilkins. 2017. 'Development of a Particulate Filter Model for the Prediction of Backpressure: Improved Momentum Balance and Entrance and Exit Effect Equations', *SAE International Journal of Engines*, 10.

Wiegmann, Andreas, Stefan Rief, and Arnulf Latz. 2006. "Soot Filtration Simulation – Generation of Porous Media on the Micro Scale from Soot Deposition on the Nano Scale." In *2nd European Conference on Filtration and Separation* Compiegne, France

Wurzenberger, Johann C., Sophie Bardubitzki, Susanne Kutschi, Robert Fairbrother, and Christoph Poetsch. 2016. 'Modeling of Catalyzed Particulate Filters - Concept Phase Simulation and Real-Time Plant Modeling on HiL', *SAE International Journal of Engines*, 9.

Xie, Luke. 2014. "3D structuring element (sphere)." In. MATLAB Central File Exchange.

Xuereb, Emilio, and Mario Farrugia. 2016. "Review and Validation of Models of Pressure Drop Across Diesel Particulate Filter and Particulate Loading Quantity." In *SAE Technical Paper Series*.

Yamamoto, Kazuhiro, and Masamichi Nakamura. 2011. 'Simulation on Flow and Heat Transfer in Diesel Particulate Filter', *Journal of Heat Transfer*, 133.

Yamamoto, Kazuhiro, and Shinya Ohori. 2012. 'Simulations on flow and soot deposition in diesel particulate filters', *International Journal of Engine Research*, 14: 333-40.

Yamamoto, Kazuhiro, Shingo Satake, Hiroshi Yamashita, Naoki Takada, and Masaki Misawa. 2006. 'Lattice Boltzmann simulation on porous structure and soot accumulation', *Mathematics and Computers in Simulation*, 72: 257-63.

Yeong, C. L. Y., and S. Torquato. 1998a. 'Reconstructing random media', *Physical Review E*, 57.

———. 1998b. 'Reconstructing random media. II. Three-dimensional media from two-dimensional cuts', *Physical Review E*, 58.

Young, Ian T. 1983. 'Image analysis and mathematical morphology, by J. Serra. Academic Press, London, 1982, xviii + 610 p. $90.00', *Cytometry*, 4: 184-85.

Zhao, F., M.-C. Lai, and D.L. Harrington. 1999. 'Automotive spark-ignited direct-injection gasoline engines', *Progress in Energy and Combustion Science*, 25: 437–562.

Zinola, Stéphane, Mickaël Leblanc, Antoinette Boreave, Badr R'Mili, Bruno Cartoixa, Philippe Vernoux, and Stéphane Raux. 2013. "The Particulate Number Emissions from GDI Engines: Advanced Characterization and Reduction through a Gasoline Particulate Filter with Membrane Technology." In *SIA International Conference : The spark Ignition Engine of the Future, At Strasbourg*.